Coastal Engineering 202 (2025) 104822

Contents lists available at ScienceDirect

Coastal Engineering

journal homepage: www.elsevier.com/locate/coastaleng

Alongshore variability in wave runup and inner surfzone wave conditions on an intermediate beach

Annika O'Dea [a,*], Britt Raubenheimer [b], Katherine Brodie [a], Steve Elgar [b]

[a] U.S. Army Engineer Research and Development Center, Field Research Facility, 1261 Duck Road, Duck, 27949, NC, USA
[b] Woods Hole Oceanographic Institution, 86 Water St, Falmouth, 02543, MA, USA

ARTICLE INFO

Keywords:
Wave runup
Swash processes
Inner surfzone processes
Lidar observations
Remote sensing

ABSTRACT

Alongshore and temporal variability in wave runup and inner surfzone wave conditions are investigated on an intermediate beach using lidar-derived elevation transect timeseries. The lidar scanners were deployed at two alongshore locations separated by ~330 m at the U.S. Army Engineer Research and Development Center Field Research Facility in Duck, NC and collected 30 min (41 min) linescan time series at 7.1 Hz (5 Hz) each hour over an 11-day period before, during, and after Hurricane Matthew in October 2016. Runup and water surface-elevation time series at the estimated 0.5-m depth contour were used to determine the extreme runup $R_{2\%}$, the mean runup and inner surfzone water surface elevation, and the significant runup and inner-surf wave heights across sea-swell, infragravity, and all frequency bands. Offshore wave conditions were determined from an array of pressure gauges located in ~8-m water depth. Results show that the significant wave height in the sea-swell frequency band H_{SS} was intermittently depth-limited in the inner surf zone, with the ratio of significant sea-swell wave height in the inner surf zone to that in about 8-m depth ($H_{SS,ISZ}/H_{SS,8\ \mathrm{m}}$) ranging from 0.42 to 1.31 during low-energy conditions and from 0.19 to 0.39 during high-energy conditions. Significant temporal variability in runup parameters was observed over the 11-day period, with $R_{2\%}$ ranging from 1.07 to 3.07 m at the southern lidar location and from 1.45 to 3.36 m at the northern lidar location. Alongshore differences in $R_{2\%}$ ranged from 0.00 to 0.90 m, with both $R_{2\%}$ and the significant swash height R_{sig} typically larger at the northern lidar location. Alongshore variability in most inner surfzone and runup parameters was largest during low-energy offshore wave conditions when the inner surf zone was unsaturated, although this trend was weakest in $R_{2\%}$. The mean runup elevation R_{mean} above the still water level was only weakly correlated with the wave-driven super-elevation of the water surface in the inner surf zone (Z_{mean}, $R^2 = 0.23$), suggesting that wave-breaking-induced setup is only one factor contributing to R_{mean}. Although the significant sea-swell swash height R_{SS} and alongshore differences in R_{SS} were correlated with foreshore beach slope $\beta_{foreshore}$ ($R^2 = 0.59$ and $R^2 = 0.70$, respectively), $R_{2\%}$, R_{mean}, and alongshore variations thereof were uncorrelated with $\beta_{foreshore}$. $R_{2\%}$ and R_{mean} were correlated with the significant wave height in the inner surf zone $H_{sig,ISZ}$ ($R^2 = 0.61$ and $R^2 = 0.72$, respectively), which is strongly influenced by wave dissipation patterns across the surf zone. These results suggest that while $\beta_{foreshore}$ affects the magnitude of swash oscillations about the mean, it has a smaller role in the total elevation reached by runup on intermediate beaches. Furthermore, the results illustrate the importance of surfzone bathymetry and the resulting temporal and alongshore variations of inner surfzone wave heights to the extreme and mean runup.

1. Introduction

Wave runup, the moving onshore edge of the ocean on the beach face, is a primary driver of beach and dune erosion during storms (Ruggiero et al., 2001; Palmsten and Splinter, 2016). Runup includes both a semi-steady component (the mean runup, measured relative to the still water level (SWL)) and a time-varying oscillatory component (sometimes referred to as swash). Runup is a key part of the total water level, a combination of runup and a SWL that includes astronomical tides and nontidal residuals, and thus is necessary to predict extreme water levels and the extent of coastal flooding during high energy events (Serafin and Ruggiero, 2014; Cohn and Ruggiero, 2016; Blenkinsopp et al., 2016). To facilitate the estimation of wave runup, a number of parametric or numerical models have been developed that rely primarily on offshore wave conditions and local beach slope (Stockdon et al., 2006;

* Corresponding author.
E-mail address: Annika.M.O'Dea@usace.army.mil (A. O'Dea).

https://doi.org/10.1016/j.coastaleng.2025.104822
Received 1 April 2025; Received in revised form 20 June 2025; Accepted 9 July 2025
Available online 21 July 2025
0378-3839/

Cox et al., 2013; Stockdon et al., 2014; Atkinson et al., 2017). However, significant scatter remains in these parameterizations, highlighting the need for ongoing observations and analyses of the contributions to and controls of runup dynamics (da Silva et al., 2020).

Observations of runup in laboratory (Miche, 1951; Hunt, 1959; Moraes, 1970; Guza and Bowen, 1977) and field (Guza and Thornton, 1982; Guza et al., 1985; Holman, 1986; Raubenheimer et al., 1995; Ruessink et al., 1998) settings have demonstrated that runup dynamics are influenced by a range of hydrodynamic and morphologic factors, with observed trends differing for different beach conditions. The beach conditions often are categorized using the Iribarren number $\xi_0 = \beta/\sqrt{H_0/L_0}$ (where β is the beach slope, H_0 is the offshore wave height, and L_0 is the offshore wavelength) (Battjes, 1974) as dissipative (low ξ_0), intermediate, and reflective (high ξ_0) (Wright and Short, 1984). In dissipative conditions with gently sloping beaches and wide surf zones, runup often is dominated by infragravity energy (R_{IG}, with a commonly-defined frequency band of $f < 0.05$ Hz), with relatively little energy at sea-swell frequencies (R_{SS}, typically $f > 0.05$ Hz) (Holman and Sallenger, 1985; Ruessink et al., 1998; Stockdon et al., 2006; Senechal et al., 2011; Hughes et al., 2014). Although R_{IG} may scale linearly with the foreshore beach slope in highly-dissipative conditions (Ruggiero et al., 2004), other studies have found that R_{IG} correlates better with offshore wave height or other metrics that do not include slope (Guza and Thornton, 1982; Raubenheimer and Guza, 1996; Ruessink et al., 1998; Ruggiero et al., 2001; Stockdon et al., 2006). R_{SS} usually is saturated in dissipative beach conditions, meaning that the swash energy in these frequency bands does not increase with increasing offshore wave energy (Miche, 1951; Huntley et al., 1977; Guza and Bowen, 1977; Guza and Thornton, 1982; Guza et al., 1985; Raubenheimer and Guza, 1996), with some work suggesting that saturation can extend into the infragravity frequency band in highly-dissipative conditions (Ruessink et al., 1998; Ruggiero et al., 2004; Senechal et al., 2011; De Bakker et al., 2014; Fiedler et al., 2015). In both reflective (steeply sloping beaches and a narrow surf zone) and intermediate conditions (representing the transition between the two end-member beach states) runup often is more energetic in the sea-swell than in the infragravity frequency band (Raubenheimer and Guza, 1996; Stockdon et al., 2006; Hughes et al., 2014). R_{SS} has been shown to be strongly related to foreshore beach slope $\beta_{foreshore}$ (Raubenheimer and Guza, 1996; Ruggiero et al., 2004; Stockdon et al., 2006) and incident wave conditions, although some studies have suggested that the nature of these relationships vary with beach state (da Silva et al., 2019).

Surfzone bathymetry affects the wave energy reaching the inner surf, which then affects the runup dynamics (Guedes et al., 2011, 2012; Senechal et al., 2018; Cohn et al., 2021). During near constant, low-energy wave conditions on an intermediate beach, significant swash height was observed to be twice as large at high than at low tide, primarily owing to reduced energy dissipation over the deeper high-tide sandbar (Guedes et al., 2011). In addition, observed moderate alongshore changes in runup height were related to alongshore variations in both beach slope and wave breaking dissipation over a sandbar with moderate alongshore morphological structure (Guedes et al., 2012). However, on a dissipative beach displaying significant alongshore morphologic variability, extreme (more than a factor of three) alongshore differences in runup height were driven primarily by morphologic differences in the inner surf zone (Senechal et al., 2018). Although these studies demonstrated the importance of surfzone bathymetry to runup dynamics on barred beaches and beaches with extreme alongshore morphologic variability, the relative importance of surfzone bathymetry, foreshore slope, and offshore wave conditions to different runup components remains unclear.

While most studies analyzing the relationships between wave conditions and runup excursions have focused on offshore wave conditions, nearshore-bathymetry-induced changes to the wave field influence runup dynamics (Guedes et al., 2011, 2012; Senechal et al., 2018; Cohn et al., 2021). Thus, a smaller number of studies have compared runup excursions to estimated breaking wave heights (Stockdon et al., 2006) or to wave conditions in the inner surf zone (Raubenheimer and Guza, 1996; Ruggiero et al., 2004; Senechal et al., 2018; Almeida et al., 2020). However, most of these studies relied on observations from in situ gauges or lidar at fixed locations which experience varying water depth through the tidal cycle. Surfzone processes are depth dependent, and thus measuring surfzone wave heights at a fixed location may introduce an apparent tidal dependence. However, using lidar linescanning timeseries to estimate wave heights at the most offshore rundown location (a roughly constant water depth) still showed strong tidal dependence of runup on wave conditions that was not reproduced by parameterizations (Brodie et al., 2012).

Here, the dependence of runup on inner surfzone and offshore wave conditions is investigated further using lidar observations collected at two alongshore locations before, during, and after Hurricane Matthew in early October 2016. The primary goals of the study are to (1) analyze the relationships between the components of runup (the extreme runup $R_{2\%}$, as well as its components R_{mean}, R_{SS}, and R_{IG}) and the inner surfzone hydrodynamic conditions, (2) quantify temporal and spatial differences in runup and inner surfzone parameters at the two locations, and (3) identify the primary factors contributing to these observed differences. In Section 2, the observation site (Section 2.1) and field datasets (Section 2.2) are described. In Section 3, the primary results are presented, including a description of the hydrodynamic conditions in the inner surf zone (Section 3.1), the factors controlling $R_{2\%}$ and the mean and oscillatory runup components (Sections 3.2 and 3.3, respectively), and the relative importance of each runup component (Section 3.4). Section 4 compares these results with existing literature and discusses potential sources of error.

2. Methods

2.1. Site description

Field data were collected at the U.S. Army Engineer Research and Development Center (ERDC) Field Research Facility (FRF) on the Outer Banks of North Carolina on the Atlantic Coast of the United States (Fig. 1). The site includes an intermediate beach with a mean foreshore of about 1:12.5, backed by partially-vegetated dunes with crest heights ranging from 6–8 m relative to the NAVD88 datum (0 m NAVD88 = −0.128 m Mean Sea Level) (Pianca et al., 2015; Cohn et al., 2021). Tides are semi-diurnal and have a typical range of about 1 m (Brodie et al., 2019). The site experiences frequent storms in the fall and winter that produce large waves and often result in rapid beach and dune evolution (Pianca et al., 2015; Brodie et al., 2019; Cohn et al., 2021). Data during an 11-day period leading up to, including, and immediately following Hurricane Matthew (2016 Oct 1–11) are used in the analysis. All data are presented in the local FRF coordinate system, with the positive x-axis pointing offshore (aligned with the FRF research pier), the positive y-axis pointing 18° west of true north, and NAVD88 as the vertical datum.

2.2. Field datasets

2.2.1. Lidar data

Two lidar scanners were deployed with an alongshore spacing of approximately 327 m, including a Riegl VZ-1000 lidar scanner (1550 nm laser) located at $y = 945$ m (O'Dea et al., 2019), referred to as the northern lidar, and a Riegl Z210 lidar scanner (904 nm laser) located at $y = 618$ m FRF, referred to as the southern lidar (Fig. 1). Starting at the top of each hour, linescan timeseries were collected by the VZ-1000 scanner at 7.1 Hz over 30-min and by the Z210 scanner at 5 Hz over 41-min, followed by three-dimensional framescans. The framescans were coregistered to a baseline (O'Dea et al., 2019) using a plane-matching technique to remove movement of the scanner between

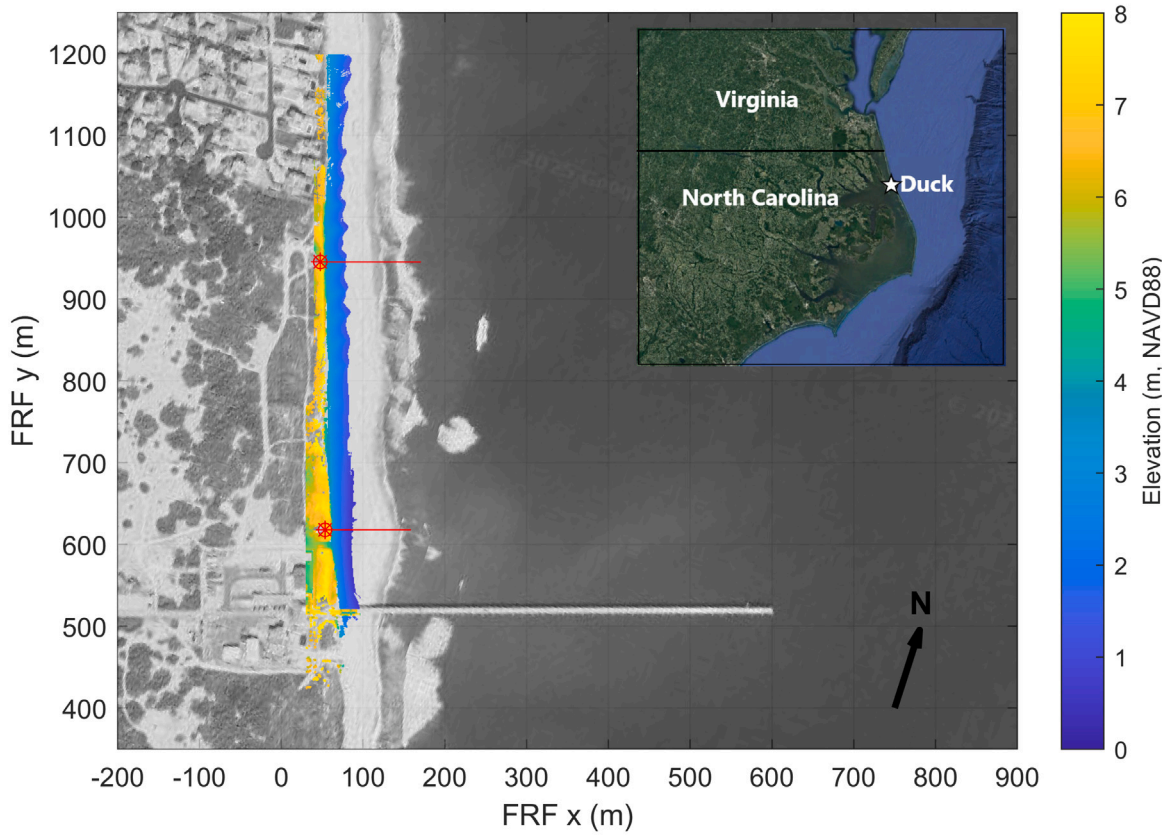

Fig. 1. Google Earth image of the field site with beach elevations (color contours, scale on the right) as a function of the alongshore and cross-shore coordinates from an example DEM from both lidar scanners (2016 Oct 5). The locations of the two lidar scanners are shown with red symbols, and an example of the cross-shore extent of the gridded lidar linescan transects are shown with red horizontal lines. A map showing the location of Duck, NC on the Atlantic coast of the United States is shown in the upper right corner.

hours. The resulting coregistration transformation matrices were used to transform spatially both the linescans and framescan for that hour into the FRF coordinate system. After coregistration, the linescan and framescan datasets were filtered and gridded at 0.1- and 1.0-m spatial resolution, respectively. Although the scanners were deployed for the entire 11-day period, some gaps occurred in the data collection owing to power outages and low data density during the storm. Sufficient data for analyses were collected during 211 of the 247 h in the deployment period (85%) at the northern lidar location and 148 of the 247 h (60%) at the southern lidar location, with the timing and duration of gaps visible in time series (Figs. 5–10).

The lidar linescan time series provide the instantaneous runup elevation, foreshore slope, and inner surfzone hydrodynamics. The instantaneous runup location was determined manually using both the elevation and reflectance returns in each of the collection periods, resulting in hourly time series of runup elevation and cross-shore location at the lidar sample rate. The hourly runup elevation time series were used to determine the 2% exceedance elevation $R_{2\%}$ (defined as the elevation exceeded by 2% of runup peaks, Stockdon et al., 2006) along with the mean runup elevation (R_{mean}). Although this parameter often is referred to as setup in the literature (e.g. Stockdon et al., 2006; da Silva et al., 2020), previous studies have hypothesized that wave-breaking-induced setup is only one factor contributing to the mean runup elevation (Nielsen, 1989; Gourlay, 1992). For this reason, the term R_{mean} was chosen to refer to the mean runup elevation. Additionally, an energy spectrum was computed from the Hamming windowed, detrended runup elevation time series, calculated using Welch's method with 4.8-min windows, 75% overlap between windows, and band averaging over three frequency bands (resulting in 36 degrees of freedom). From the spectrum, the significant swash heights over all frequencies (R_{sig}), the sea-swell band (R_{SS}, $f > 0.05$ Hz), and the infragravity band (R_{IG}, $f \leq 0.05$ Hz) were computed as $R = 4\sqrt{\int PSD}$, where PSD is the runup elevation spectrum, with the integration occurring only over the frequency bands of interest. A combined mean and oscillatory runup parameter R_T was defined as $R_T = \frac{1}{2}R_{sig} + R_{mean}$. A list of variable names and definitions is provided in Table 1.

The manual digitization process separated each gridded linescan transect into grid cells classified as beach (shoreward of the instantaneous runup location) and as water (seaward of the instantaneous runup location). For each hourly collection period, a mean foreshore transect was determined using only grid cells classified as beach and a mean water surface elevation transect was determined using only grid cells classified as water (Fig. 2). The mean foreshore transect was used to extract the hourly mean foreshore slope ($\beta_{foreshore}$), defined as the slope of the best-fit linear trend to the beach elevation profile in the region defined by the mean horizontal swash position ± two standard deviations (Ruggiero et al., 2001; Stockdon et al., 2006).

In addition to the runup elevation time series, a water surface elevation time series was extracted at the time-varying location of the estimated 0.5-m depth contour each hour (hereafter referred to as the inner surfzone time series). The mean foreshore transect determined from the linescan time series extended only to the offshore edge of the swash zone. To estimate depth contours in the inner surf zone, the mean foreshore transect was linearly extended using the average linear slope over the final 3 m of the mean foreshore, and the extended mean foreshore at each cross-shore location was subtracted from the mean water surface elevation at that location (Fig. 2). The 0.5-m depth contour was selected as it was the approximate average estimated depth of the first grid cell beyond the offshore extent of the swash zone.

Table 1
Variable names, definitions, and relevant locations.

Variable	Definition	Location
$H_{sig,8\ m}$	Significant wave height over all frequencies	~8-m depth
$H_{SS,8\ m}$	Significant wave height over sea-swell frequencies	~8-m depth
$H_{IG,8\ m}$	Significant wave height over infragravity frequencies	~8-m depth
$H_{sig,ISZ}$	Significant wave height over all frequencies	Inner surf zone
$H_{SS,ISZ}$	Significant wave height over sea-swell frequencies	Inner surf zone
$H_{IG,ISZ}$	Significant wave height over infragravity frequencies	Inner surf zone
$H_{f<0.1\ Hz,ISZ}$	Significant wave height over frequencies < 0.1 Hz	Inner surf zone
Z_{mean}	Mean water surface elevation	Inner surf zone
$R_{2\%}$	2% exceedance runup elevation	Swash zone
R_{sig}	Significant runup height over all frequencies	Swash zone
R_{SS}	Significant runup height over sea-swell frequencies	Swash zone
R_{IG}	Significant runup height over infragravity frequencies	Swash zone
R_{mean}	Mean runup elevation	Swash zone
R_T	Combined mean and oscillatory runup ($\frac{1}{2}R_{sig} + R_{mean}$)	Swash zone

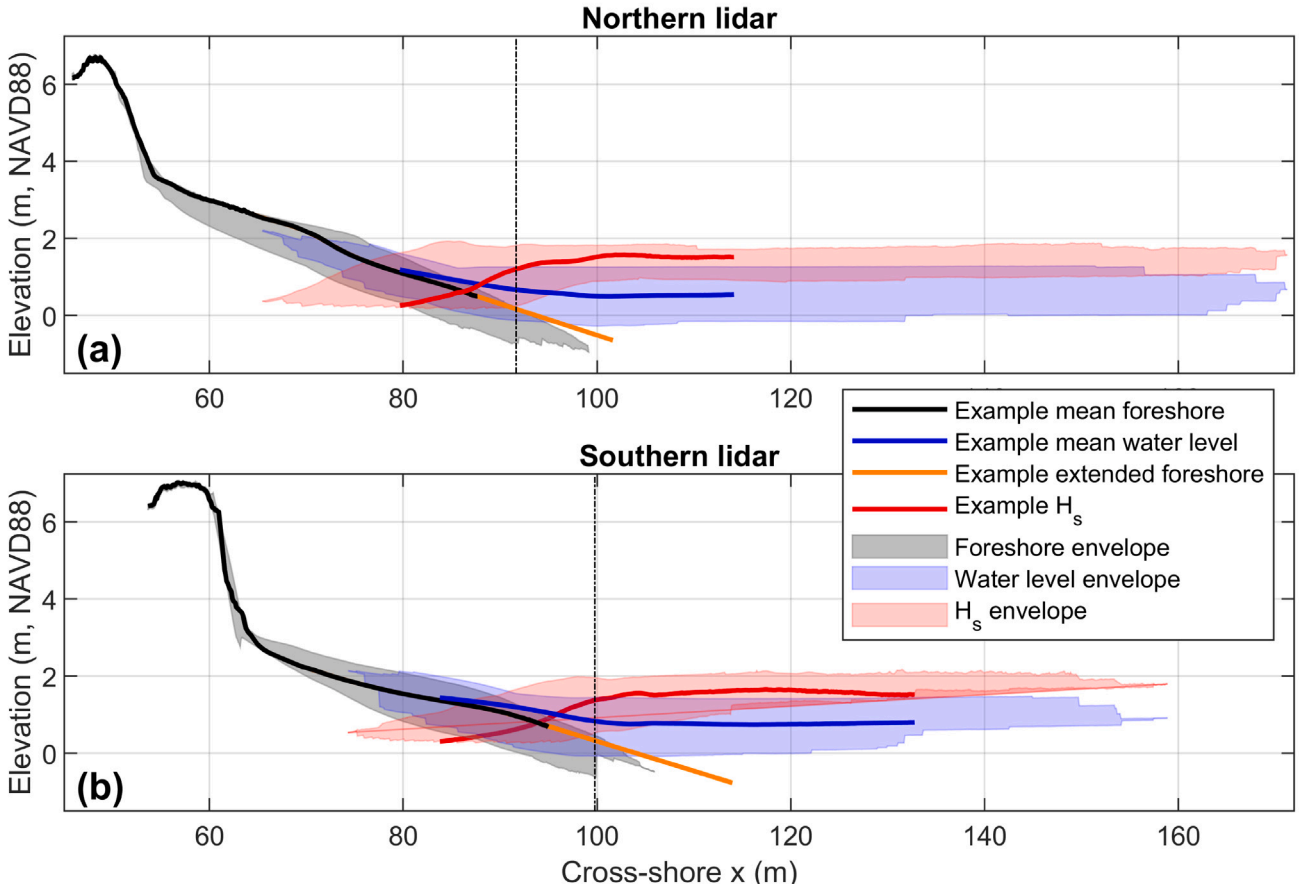

Fig. 2. Mean foreshore elevation (gray shaded), mean water surface elevation (blue shaded), and significant wave height (red shaded) envelopes versus cross-shore coordinate from all lidar linescan collections, along with an example mean water surface elevation (blue solid curve), mean foreshore (black solid curve), foreshore extension used to estimate depth (orange solid line), and significant wave height (red solid curve) from an example hour on 2016 Oct 5 00:00 UTC for the (a) northern and (b) southern lidars. Black dot-dashed vertical lines show the locations of the estimated 0.5-m contour corresponding to the example hour.

The inner surfzone water surface-elevation time series was used to compute the inner surfzone (0.5-m depth) mean water surface elevations (Z_{mean}) and energy spectra following the same methodology as for the runup spectra. The spectra were used to determine the inner surfzone significant wave height over all frequencies ($H_{sig,ISZ}$), sea-swell frequencies ($H_{SS,ISZ}$), and infragravity frequencies ($H_{IG,ISZ}$).

2.2.2. Bathymetry surveys

The bathymetry was surveyed on 2016 September 26 (pre-Hurricane Matthew) and 2016 October 20 (post-Hurricane Matthew) using a digital echosounder and RTK-GPS mounted to a 10-m long amphibious vehicle (LARC) (Forte et al., 2017) (Fig. 3). Transect lines with roughly 50-m alongshore spacing were collected from the dune toe to 8-m water depth, along with additional transect lines with 100–200 m alongshore spacing extending to 15-m water depth.

2.2.3. Hydrodynamic conditions

Nearshore hydrodynamic conditions were determined from an array of bottom-mounted pressure gauges located in approximately 8-m water depth, which provided estimates of the full frequency-directional wave spectrum each hour (Long and Oltman-Shay, 1991). The frequency-directional wave spectra were used to determine the significant wave height over all frequencies ($H_{sig,8\ m}$), sea-swell frequencies ($H_{SS,8\ m}$), and infragravity frequencies ($H_{IG,8\ m}$), along with the peak

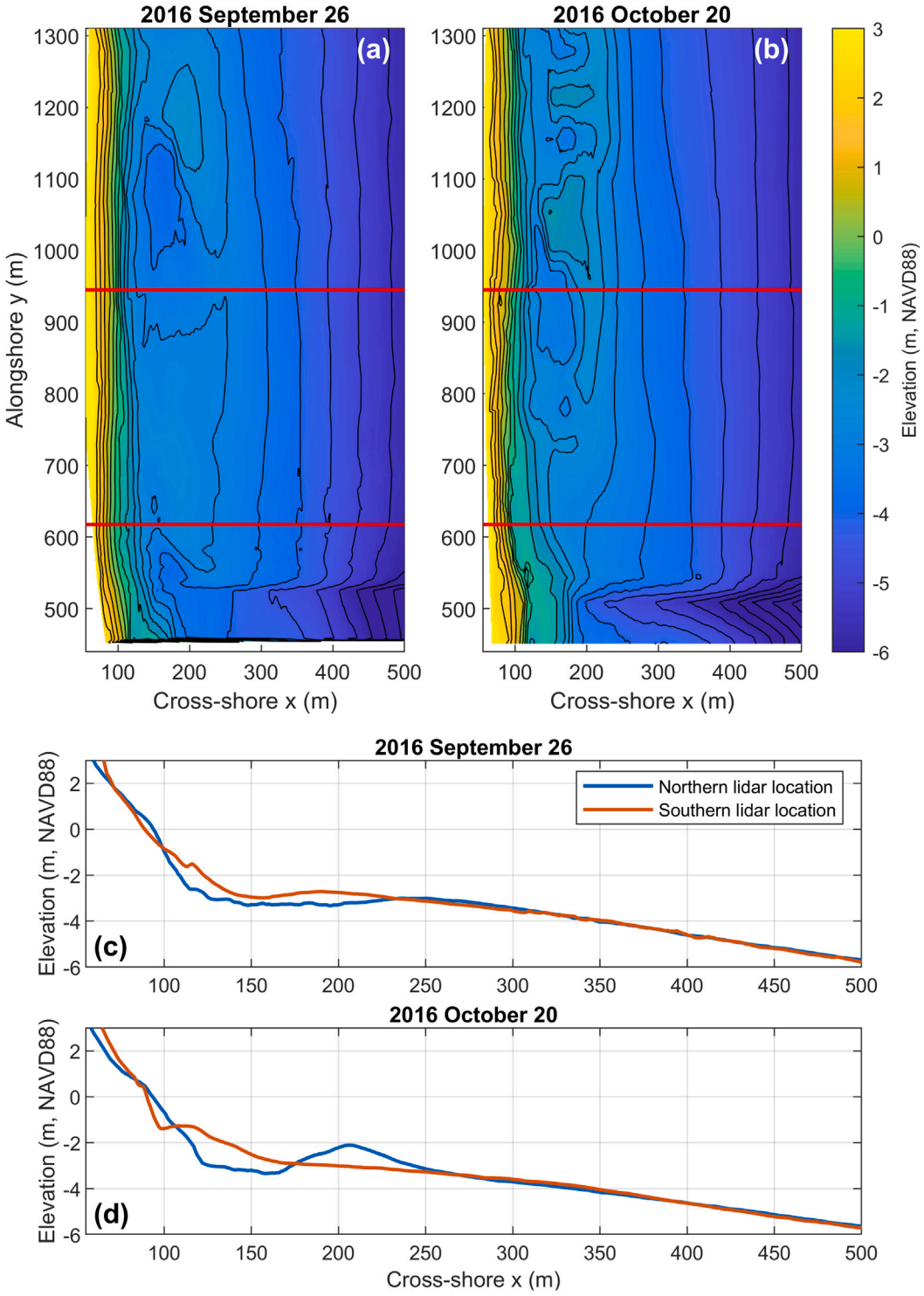

Fig. 3. (a,b) Contours of seafloor elevation (scale on the right) as a function of alongshore and cross-shore distances from bathymetric surveys collected on (a) 2016 Sept 26 and (b) 2016 Oct 20 (before and after Hurricane Matthew), and (c,d) elevation versus cross-shore distance along transects at the alongshore locations of the northern (blue curves) and southern (red curves) lidars on (c) 2016 Sept 26 and (d) 2016 Oct 20. The alongshore locations of the transects shown in (c,d) are indicated with red horizontal lines in (a,b).

and mean period (T_p and T_m, respectively), and peak and mean wave direction (θ_p and θ_m, respectively) (Fig. 4). Offshore significant wave height (H_0) was calculated by deshoaling $H_{sig,8\ \mathrm{m}}$ to deep water using linear wave theory. Offshore wavelength L_0 was determined using the peak period T_p from the 8-m array following linear wave theory (with $L_0 = gT_p^2/2\pi$). Water levels were determined from a tide gauge at the end of the FRF pier.

3. Results

3.1. Nearshore and inner surfzone wave conditions

To quantify differences in the wave conditions in the inner surfzone relative to those on the inner shelf, significant wave heights in 0.5-m ($H_{sig,ISZ}$, $H_{SS,ISZ}$, and $H_{IG,ISZ}$) and 8-m water depth ($H_{sig,8\ \mathrm{m}}$, $H_{SS,8\ \mathrm{m}}$, and $H_{IG,8\ \mathrm{m}}$) were compared with each other (Fig. 5). Over

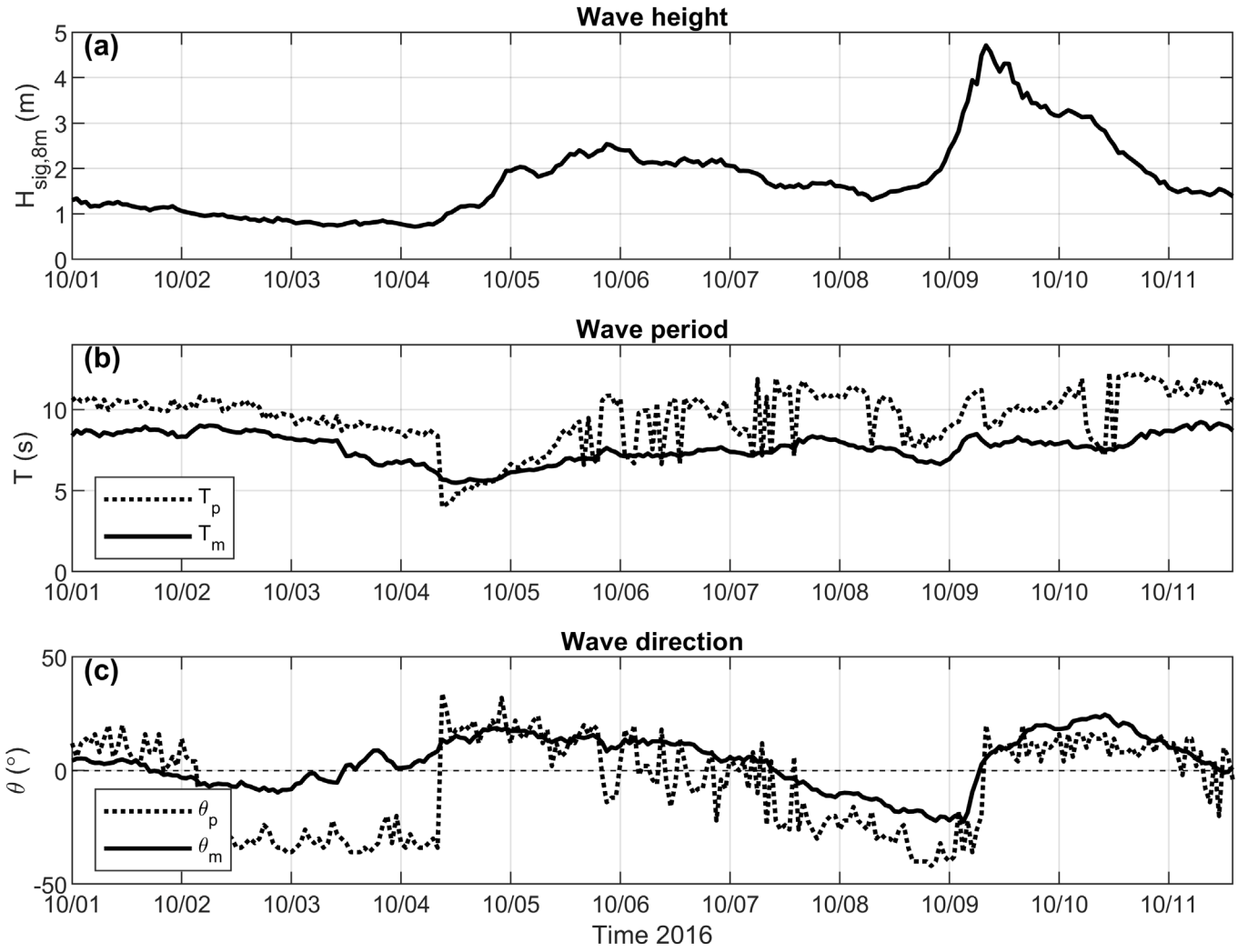

Fig. 4. (a) Significant wave height $H_{sig,8\ m}$, (b) mean (solid curve) and peak (dotted curve) wave period T, and (c) mean (solid curve) and peak (dotted curve) wave direction θ in 8-m depth versus time (2016 Oct 1–11). Wave directions are given in a Cartesian coordinate system, with 0 indicating shore normal, positive values indicating an approach from the North, and negative values indicating an approach from the South.

the entire time series, $H_{sig,ISZ}$ was correlated weakly with $H_{sig,8\ m}$ (R^2 = 0.27, Fig. 5a,d). There was significantly more variability in the magnitude of $H_{sig,8\ m}$ than in the magnitude $H_{sig,ISZ}$ at either lidar location over the 11-day study period, with $H_{sig,8\ m}$ ranging from 0.72 to 4.71 m and $H_{sig,ISZ}$ ranging from 0.86 to 1.50 m at the northern lidar and 0.53 to 1.47 m at the southern lidar (Fig. 5a,d). The largest differences in the magnitudes of $H_{sig,8\ m}$ and $H_{sig,ISZ}$ were observed during the peak of the storm on 2016 Oct 9 (with $H_{sig,ISZ} < 1.5$ m at both lidar locations and $H_{sig,8\ m} > 4.5$ m). As $H_{sig,8\ m}$ increased over about 2 m, $H_{sig,ISZ}$ asymptoted to about 1.25 ± 0.25 m, suggesting that wave breaking in the mid and outer surfzone resulted in energy saturation in the inner surf zone during the storm (Fig. 5a,d). During smaller wave conditions (1–4 October), $H_{sig,8\ m}$ was smaller than $H_{sig,ISZ}$ at the northern site and similar to $H_{sig,ISZ}$ at the southern site (Fig. 5a), with a tidal signal at the southern site.

The majority of the wave energy at the 8-m array was located in the sea-swell bands, with the ratio of sea-swell to infragravity energy ($H_{SS,8\ m}/H_{IG,8\ m}$) ranging from 7.1 to 18.7, with a mean of 10.3. In the inner surf zone, the ratio of sea-swell to infragravity energy ($H_{SS,ISZ}/H_{IG,ISZ}$) was significantly smaller due to an increase in infragravity energy and often a decrease in sea-swell energy closer to shore, with a mean $H_{SS,ISZ}/H_{IG,ISZ}$ of 2.4 at both lidar locations. Although the mean $H_{SS,ISZ}/H_{IG,ISZ}$ values were similar at the two lidar locations, the range was larger at the northern lidar location (1.0 to 4.9) than at the southern lidar location (1.1 to 3.8). The trends in the $H_{SS,ISZ}$ and $H_{SS,8\ m}$ closely followed the trends in $H_{sig,ISZ}$ and $H_{sig,8\ m}$, respectively, with a similarly weak correlation between $H_{SS,ISZ}$ and $H_{SS,8\ m}$ (R^2 = 0.10) (Fig. 5b,e). In contrast to the sea-swell band, the $H_{IG,ISZ}$ correlated well with $H_{IG,8\ m}$ (R^2 = 0.76) (Fig. 5c,f), with magnitudes of $H_{IG,ISZ}$ around 1.2 to 4.8 times the magnitude of $H_{IG,8\ m}$.

3.2. $R_{2\%}$ and R_T

The $R_{2\%}$ elevations ranged from 1.07 to 3.07 m at the southern lidar location and 1.45 to 3.36 m at the northern lidar location (Fig. 6). $R_{2\%}$ usually was larger at the northern lidar location, although the difference in magnitude varied significantly through time, with a maximum difference in $R_{2\%}$ ($\Delta R_{2\%}$) between the two locations of 0.9 m (1 October 05:00 UTC). From 2016 Oct 1–5, $R_{2\%}$ at the southern lidar location had a strong tidal signal, with $R_{2\%}$ an average of 32% larger at high tide compared with that at the subsequent low tide. During this same period, there was no clearly-defined and consistent tidal signal in $R_{2\%}$ at the northern lidar location. There was a tidal signal at the northern lidar location from 2016 Oct 5–11 (Fig. 6c, blue curve). Due to gaps in the time series, it is not known if there was a consistent tidal signal at the southern lidar location during much of this period (Fig. 6c, red curve).

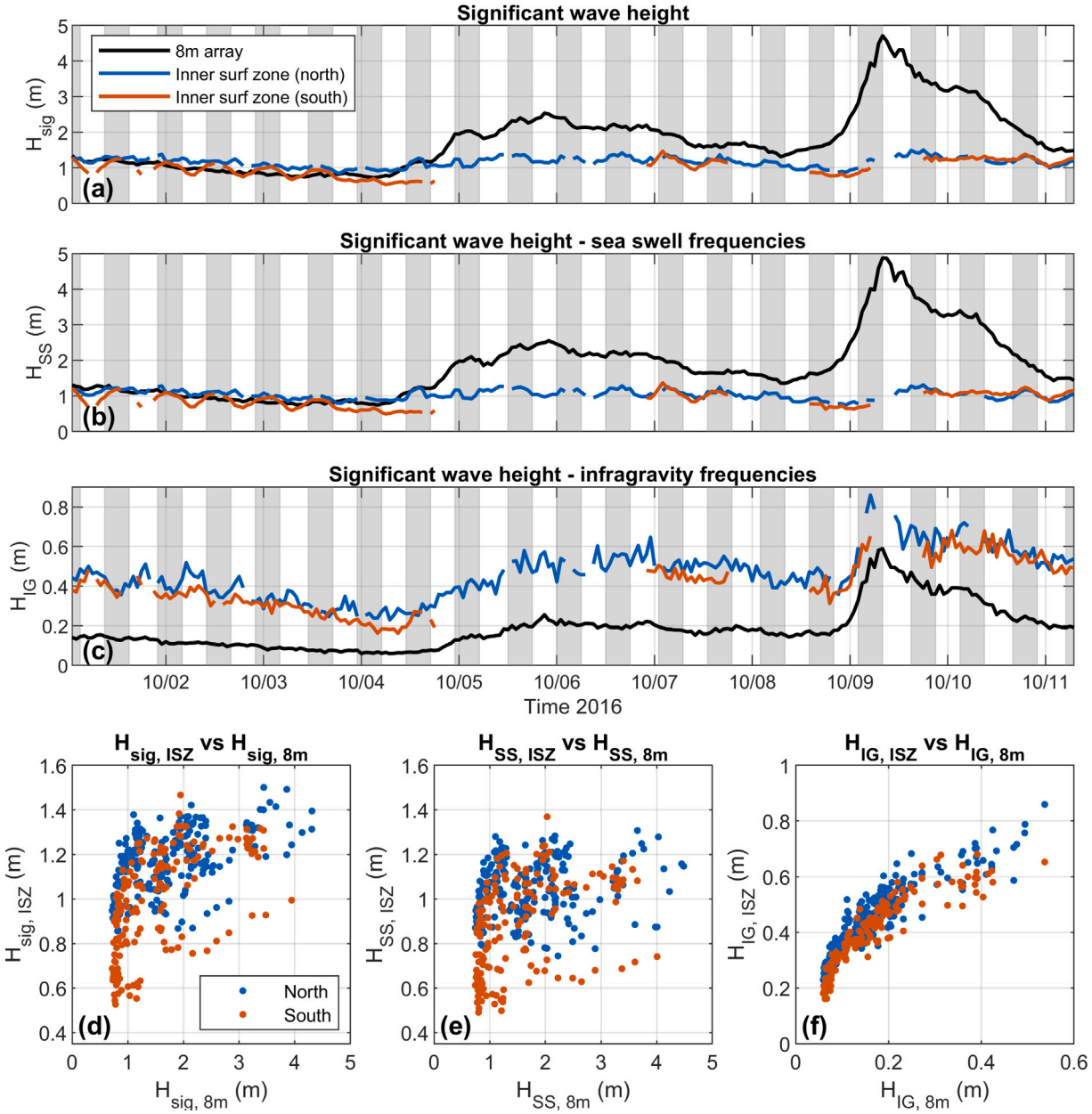

Fig. 5. Significant wave height at the 8-m array (black curves) and in the inner surf zone at the northern (blue curve) and the southern (red curve) lidar locations over (a) all frequencies, (b) sea-swell frequencies, and (c) infragravity frequencies versus time in 2016, and (d) $H_{sig,ISZ}$ versus $H_{sig,8\ m}$, (e) $H_{SS,ISZ}$ versus $H_{SS,8\ m}$, and (f) $H_{IG,ISZ}$ versus $H_{IG,8\ m}$.

$R_{2\%}$ was correlated with the total wave energy in the inner surf zone $H_{sig,ISZ}$ ($R^2 = 0.61$, Fig. 6a) and with total offshore wave energy $H_{sig,8\ m}$ ($R^2 = 0.47$, Table 2), but the strongest correlation was found between $R_{2\%}$ and the significant wave height in the inner surf zone integrated over all frequency bands below 0.1 Hz $H_{f<0.1\ Hz,ISZ}$ ($R^2 = 0.81$, Table 2). However, there was no correlation between the difference in $R_{2\%}$ at the two lidar locations and the difference in $H_{f<0.1\ Hz,ISZ}$ or $H_{sig,ISZ}$ ($R^2 = 0.11$ and $R^2 = 0.02$, respectively), suggesting that the difference in wave energy at the base of the foreshore alone is not a primary driver of the differences in $R_{2\%}$ at the two sites. There was no correlation between $R_{2\%}$ and $\beta_{foreshore}$ ($R^2 = 0.02$). $R_{2\%}$ was correlated with an estimated $R_{2\%}$ determined using the Stockdon extreme runup parameterization (Stockdon et al., 2006) ($R^2 = 0.59$), but the parameterized runup values with the published coefficients consistently under-predicted the measured runup magnitude, with a bias of 0.85 m over the entire study period.

Consistent with previous results (Stockdon et al., 2006), R_T was smaller than $R_{2\%}$ throughout the deployment period (with a mean difference of 0.36 m and a best fit line of $y = 1.07x + 0.24$), but followed similar spatial and temporal trends (Fig. 6c, Table 2). The largest differences between $R_{2\%}$ and R_T were observed during the storm, with a maximum difference of 1.15 m. To explore the drivers of the observed temporal and spatial differences in $R_{2\%}$ and R_T, runup was separated into a mean value and the sea-swell and infragravity swash components, and the factors influencing each component were analyzed individually.

3.3. Runup components

3.3.1. R_{mean}

The mean runup R_{mean} varied from 0.56 to 1.59 m at the location of the northern lidar and from 0.37 to 1.52 m at the location of the

Table 2
Correlations coefficients R^2, slopes m, and intercepts b from linear regressions between dependent (runup) variables and independent variables. Δ indicates the absolute difference between the parameter at the northern and southern lidar locations.

Dependent variable	Independent variable	m	b	R^2
$R_{2\%}$	$H_{sig,8\ \mathrm{m}}$	0.42	1.39	0.47
$R_{2\%}$	$H_{sig,ISZ}$	1.76	0.16	0.61
$R_{2\%}$	$H_{IG,ISZ}$	3.14	0.72	0.72
$R_{2\%}$	$H_{f<0.1\ \mathrm{Hz},ISZ}$	2.39	0.38	0.81
$R_{2\%}$	$\beta_{foreshore}$	4.13	1.69	0.02
$R_{2\%}$	Stockdon	0.72	−0.27	0.59
$\Delta R_{2\%}$	$\Delta H_{f<0.1\ \mathrm{Hz},ISZ}$	0.89	0.21	0.11
R_T	$H_{sig,8\ \mathrm{m}}$	0.32	1.19	0.35
R_T	$H_{sig,ISZ}$	1.59	−0.02	0.65
R_T	$H_{IG,ISZ}$	2.71	0.54	0.69
R_T	$H_{f<0.1\ \mathrm{Hz},ISZ}$	2.15	0.19	0.84
R_T	$\beta_{foreshore}$	3.70	1.37	0.02
ΔR_T	$\Delta H_{f<0.1\ \mathrm{Hz},ISZ}$	1.23	0.17	0.19
R_{mean}	$H_{sig,ISZ}$	1.10	−0.26	0.72
R_{mean}	Z_{mean}	0.83	0.77	0.23
R_{mean}	$\beta_{foreshore}$	−2.60	1.15	0.02
R_{mean}	$\beta_{foreshore}\sqrt{H_0 L_0}$	0.27	0.58	0.24
ΔR_{mean}	$\Delta H_{sig,ISZ}$	0.61	−0.01	0.43
R_{SS}	$H_{SS,ISZ}$	0.27	0.81	0.03
R_{SS}	$\beta_{foreshore}$	14.96	−0.22	0.59
R_{SS}	$\beta_{foreshore}\sqrt{L_0}$	0.93	0.13	0.68
R_{SS}	$\beta_{foreshore}\sqrt{H_0 L_0}$	0.41	0.56	0.41
ΔR_{SS}	$\Delta\beta_{foreshore}$	14.7	0.07	0.70
R_{IG}	$H_{IG,ISZ}$	1.71	0.19	0.62
R_{IG}	$H_{IG,8\ \mathrm{m}}$	1.87	0.61	0.39
R_{IG}	$H_{sig,ISZ}$	0.99	−0.14	0.56
R_{IG}	$H_{sig,8\ \mathrm{m}}$	0.21	0.60	0.32
R_{IG}	$\sqrt{H_0 L_0}$	0.04	0.37	0.44
ΔR_{IG}	$\Delta H_{IG,ISZ}$	0.93	0.24	0.09
R_{sig}	$H_{sig,ISZ}$	0.96	0.49	0.28
R_{sig}	$H_{IG,ISZ}$	2.08	0.65	0.48
R_{sig}	$H_{f<0.1\ \mathrm{Hz},ISZ}$	1.58	0.65	0.54
R_{sig}	$\beta_{foreshore}$	12.6	0.43	0.30
R_{sig}	$\beta_{foreshore}H_{IG,ISZ}$	22.8	0.69	0.73
R_{sig}	$\beta_{foreshore}\sqrt{H_0 L_0}$	0.58	0.79	0.59
ΔR_{sig}	$\Delta\beta_{foreshore}$	11.2	0.18	0.53

southern lidar (Fig. 7). Similar to $H_{sig,ISZ}$, from October 1–5 the tidal signal in R_{mean} was stronger at the location of the southern than at the northern lidar. The peak in R_{mean} through the tidal cycle occurred slightly before the high tide from October 1–4. R_{mean} was correlated with the significant wave height in the inner surf zone $H_{sig,ISZ}$ (R^2 = 0.72, Fig. 7a,b, Table 2). Additionally, the difference in R_{mean} at the two lidar locations was correlated with the difference in $H_{sig,ISZ}$ (R^2 = 0.43, Fig. 7c), suggesting that the difference in inner surfzone wave energy at the two lidar locations is contributing to the observed differences in R_{mean}. Although there was only a weak correlation between R_{mean} and the mean water surface elevation in the inner surf zone Z_{mean} (R^2 = 0.23, Fig. 7b), there was a stronger correlation between the residuals in the relationship between R_{mean} and $H_{sig,ISZ}$ and Z_{mean} (R^2 = 0.48, Fig. 7d), suggesting that Z_{mean} had a secondary influence on R_{mean}. There was no correlation between R_{mean} and $\beta_{foreshore}$ (R^2 = 0.02, not shown), and R_{mean} was correlated only weakly with the commonly-used parameterization $\beta_{foreshore}\sqrt{H_0 L_0}$ (R^2 = 0.24, Table 2) (Stockdon et al., 2006).

3.3.2. R_{sig}, R_{SS}, and R_{IG}

The significant swash height in the sea-swell band R_{SS} typically was larger at the northern lidar location, with a range of 0.62 to 2.28 m (versus a range of 0.53 to 1.43 m at the southern lidar location) (Fig. 8e,f). Spatial differences in $\beta_{foreshore}$ was a primary driver of the observed differences in R_{SS} at the two lidar locations (R^2 = 0.70, Fig. 8a,c). R_{SS} was not correlated with $H_{SS,ISZ}$ (R^2 = 0.03, Fig. 8b). However, there was a weak correlation between the residuals in the relationship between R_{SS} and $\beta_{foreshore}$ and $H_{sig,ISZ}$ (R^2 = 0.26, Fig. 8c), suggesting that the inner surfzone wave energy has a secondary influence on R_{SS}. The correlation between R_{SS} and $\beta_{foreshore}$ alone (Fig. 8a) was better than the correlation between R_{SS} and the commonly-used parameterization $\beta_{foreshore}\sqrt{H_0 L_0}$ (R^2 = 0.59 and R^2 = 0.41, respectively) (Stockdon et al., 2006), although the strongest correlation of the parameters tested was between R_{SS} and $\beta_{foreshore}\sqrt{L_0}$ (R^2 = 0.68).

Similar to R_{SS}, the significant swash height in the infragravity band R_{IG} often was larger at the northern lidar location (0.55 to 1.58 m) than at the southern lidar location (0.39 to 1.30 m) (Fig. 9a,b). There was a stronger correlation between R_{IG} and $H_{IG,ISZ}$ (R^2 = 0.62, Fig. 9a) than with $H_{IG,8\ \mathrm{m}}$ (R^2 = 0.39, Fig. 9b), $H_{sig,8\ \mathrm{m}}$ (R^2 = 0.32, not shown), or $\sqrt{H_0 L_0}$ (R^2 = 0.44, not shown). From October 1–4, there is significant tidal variability in R_{IG} at both lidar locations, with larger R_{IG} occurring at high tide compared with that during the subsequent low tide (Fig. 9c, solid curves). There is no clear tidal signal in $H_{IG,ISZ}$ at the southern lidar location during the same time period, and a small inverted tidal signal in $H_{IG,ISZ}$ at the northern lidar location, with increased $H_{IG,ISZ}$ occurring at low tide (Fig. 9c, dashed curves).

The significant swash height over all frequency bands R_{sig} was correlated with both $\beta_{foreshore}$ (R^2 = 0.30) and $H_{IG,ISZ}$ (R^2 = 0.48), with the R^2 increasing to 0.73 when the parameters were combined ($\beta_{foreshore}H_{IG,ISZ}$). However, the difference in R_{sig} at the two lidar locations primarily was controlled by differences in beach slope (R^2 = 0.53).

3.4. Relative importance of runup components

The relative importance of the mean and swash components, given by the ratio of R_{mean} to $\frac{1}{2}R_{sig}$, ranged from 0.8 to 1.9 at the northern lidar location and from 0.9 to 2.3 at the southern lidar location (Fig. 10a). There was a tidal signal in $R_{mean}/\frac{1}{2}R_{sig}$, which peaked during the rising tides from Oct 1–4 (Fig. 10a). R_{SS} was larger than R_{IG} about

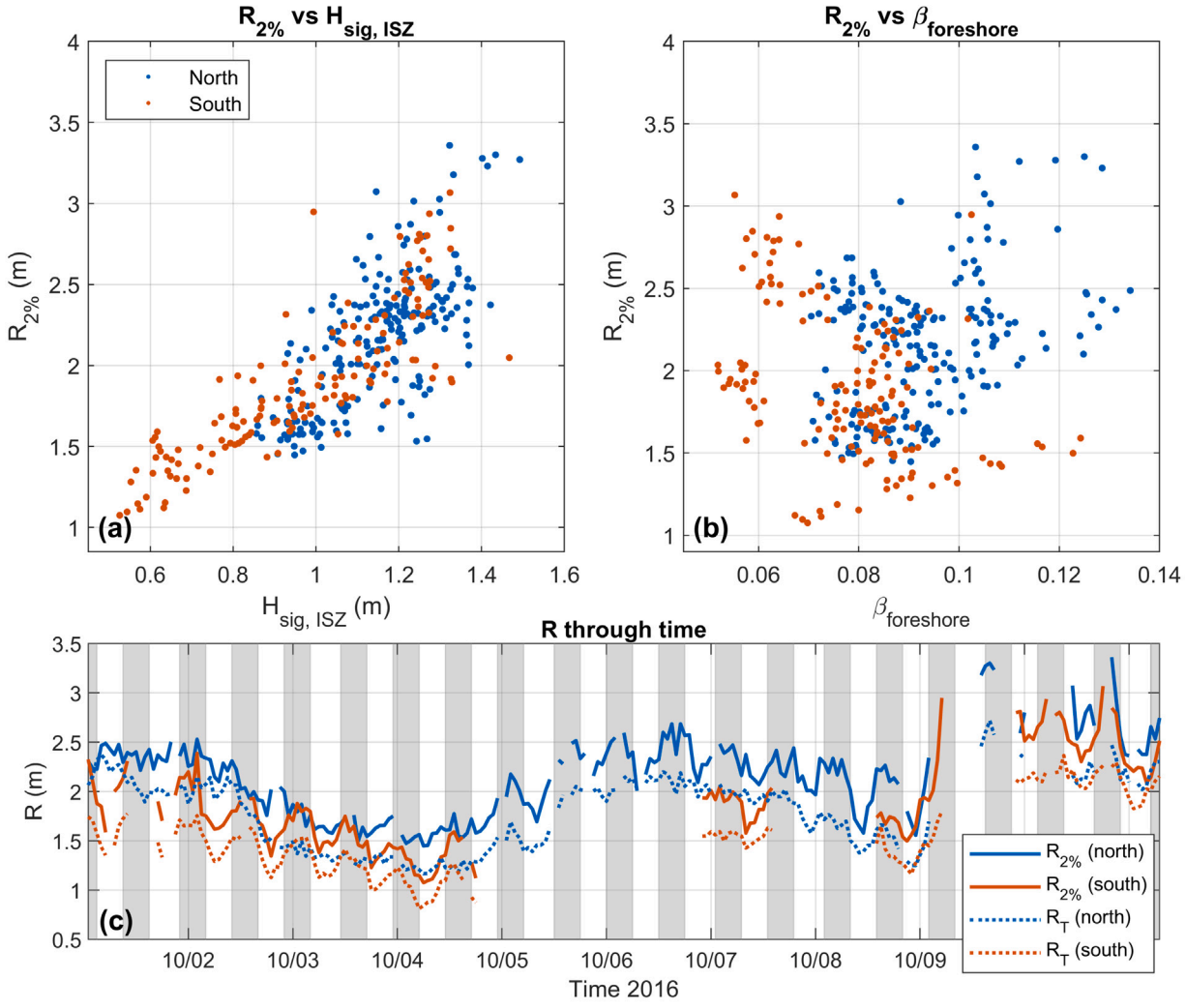

Fig. 6. $R_{2\%}$ versus (a) $H_{sig,ISZ}$ and (b) $\beta_{foreshore}$, and (c) $R_{2\%}$ (solid curves) and $R_T = \frac{1}{2}R_{sig} + R_{mean}$ (dotted curves) versus time at the northern (blue) and southern (red) lidar locations. Gray shaded regions show the 3 h leading up to and 3 h following high tide.

3/4 of the time at both lidar locations, with $R_{SS}/R_{IG} > 1$ during 156 out of 214 h at the northern lidar location and 112 out of 151 h at the southern lidar location (Fig. 10b). However, the range of R_{SS}/R_{IG} values was larger at the southern lidar location, with R_{IG} reaching 1.6 times the value of R_{SS} (Oct 7). The lowest R_{SS}/R_{IG} values (<0.65) were all at the southern lidar location, and corresponded to times with unusually gentle slopes (0.052 to 0.068) and small R_{SS} (0.60 to 0.85 m). Prior to the storm (Oct 1–5), the ratio of sea-swell to infragravity energy in the inner surf zone $H_{SS,ISZ}/H_{IG,ISZ}$ had a strong tidal signal at both lidar locations, with $H_{SS,ISZ}/H_{IG,ISZ}$ peaking near high tide (Fig. 10c,d, black curves). However, the trends in R_{SS}/R_{IG} during this same period followed the trends in $\beta_{foreshore}$, resulting in R_{SS}/R_{IG} values that were often out of phase with $H_{SS,ISZ}/H_{IG,ISZ}$ (Fig. 10c,d, compare solid colored with black curves).

4. Discussion

4.1. Role of incident conditions

The relationship between wave conditions in 8-m water depth and in the inner surf zone varied significantly (Fig. 5). To understand these differences and how they influenced runup dynamics, subsets of the time series representing small (October 1–4) and large (October 9–10) offshore wave conditions were analyzed separately.

4.1.1. October 1–4

When offshore wave heights $H_{SS,8\ m}$ ranged between 0.75 and 1.35 m (low to moderate incident waves), significant alongshore and temporal variability was observed in some inner surfzone and runup parameters. During low to moderate waves, the ratio of $H_{SS,IZ}$ to $H_{SS,8\ m}$ had a much larger range (0.42 to 1.31) than during higher energy offshore conditions (0.19 to 0.80 for $H_{SS,8\ m}$ >1.35 m) (Fig. 11). $H_{SS,IZ}$ exceeded $H_{SS,8\ m}$ during 61 of the total collection hours at the northern lidar location and 20 of the total collection hours at the southern lidar location (Fig. 11). Differences in $H_{SS,ISZ}$ between the two lidar locations ranged from 0.00 to 0.68 m, compared with 0.00 to 0.23 m during times with larger offshore wave conditions (Fig. 12). The large alongshore variability of waves in 0.5-m water depth suggests that energy in the sea-swell frequency band often was unsaturated (or intermittently saturated) in the inner surf zone during this time period, with alongshore varying surfzone dissipation due to alongshore variable bathymetry.

Inner surfzone parameters have a strong tidal signature at the southern lidar location during the low to moderate waves (both $H_{sig,ISZ}$ and $H_{SS,ISZ}$), with a more subtle and at times different tidal signal at the northern lidar location (Fig. 5). On beaches with non-planar cross-shore morphology, changes in water level through the tidal cycle affect both the beach slope in the swash zone (as the location of the swash zone moves due to changing water levels), as well as the location of wave breaking (e.g., on or offshore of a sandbar or on

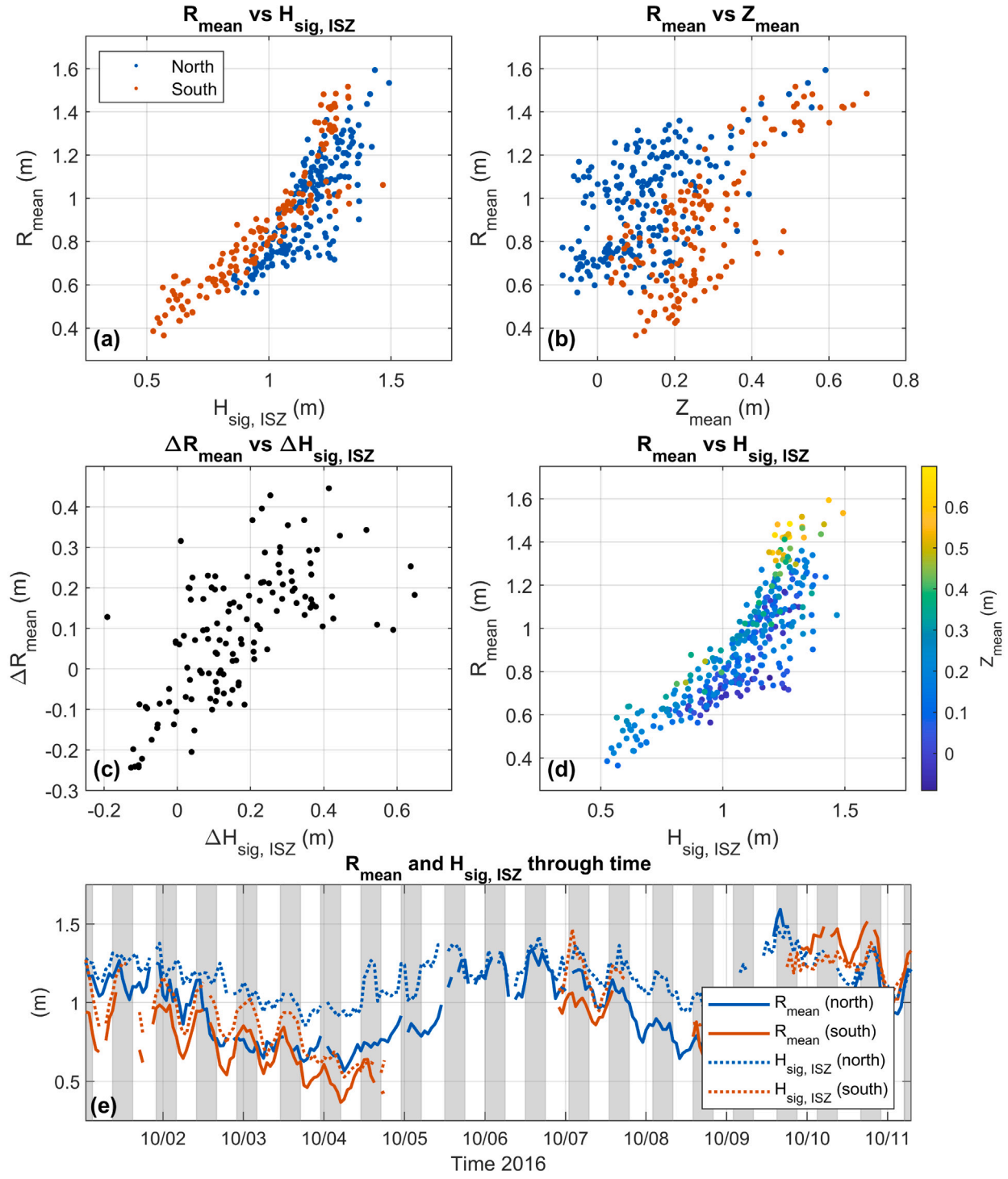

Fig. 7. R_{mean} versus (a) $H_{sig,ISZ}$ and (b) Z_{mean}, (c) the difference in R_{mean} at the two alongshore locations versus the difference in $H_{sig,ISZ}$ at the two alongshore locations, (d) R_{mean} versus $H_{sig,ISZ}$ colored by Z_{mean} (scale on right), and (e) R_{mean} (solid curves) and $H_{sig,ISZ}$ (dashed curves) versus time at the northern (blue) and southern (red) lidars.

the foreshore) and surfzone width (Chen et al., 2024). Although the inner surfzone wave energy was of a similar magnitude at the two lidar locations at high tide during low to moderate waves, $H_{sig,ISZ}$ was smaller at the southern lidar location during low tide (Figs. 5b, 7e), suggesting stronger low-tide surfzone dissipation at the southern site. The spatial breaking patterns visible in optical imagery collected using an ARGUS camera system (Holman and Stanley, 2007) at high tide were similar, with a relatively narrow surf zone (~20 m) and an initiation of breaking around x = 100 m (Fig. 13a,c). Although some breaking was visible on the flat terrace extending to around x = 275 m at both lidar locations at low-tide when the brightest intensity at each location in ARGUS imagery was visualized, the primary difference between the two locations appears to be a widening of the surf zone and a slight offshore shift in breaking location at the southern lidar location (time-averaged ARGUS imagery shown in Fig. 13b,d) due to a shallower region (100 < x < 140 m, with a maximum depth difference of 1.1 m) at the offshore edge of the surf zone (Fig. 13e). Although the bathymetry did not exhibit strong alongshore variability (Senechal et al., 2018),

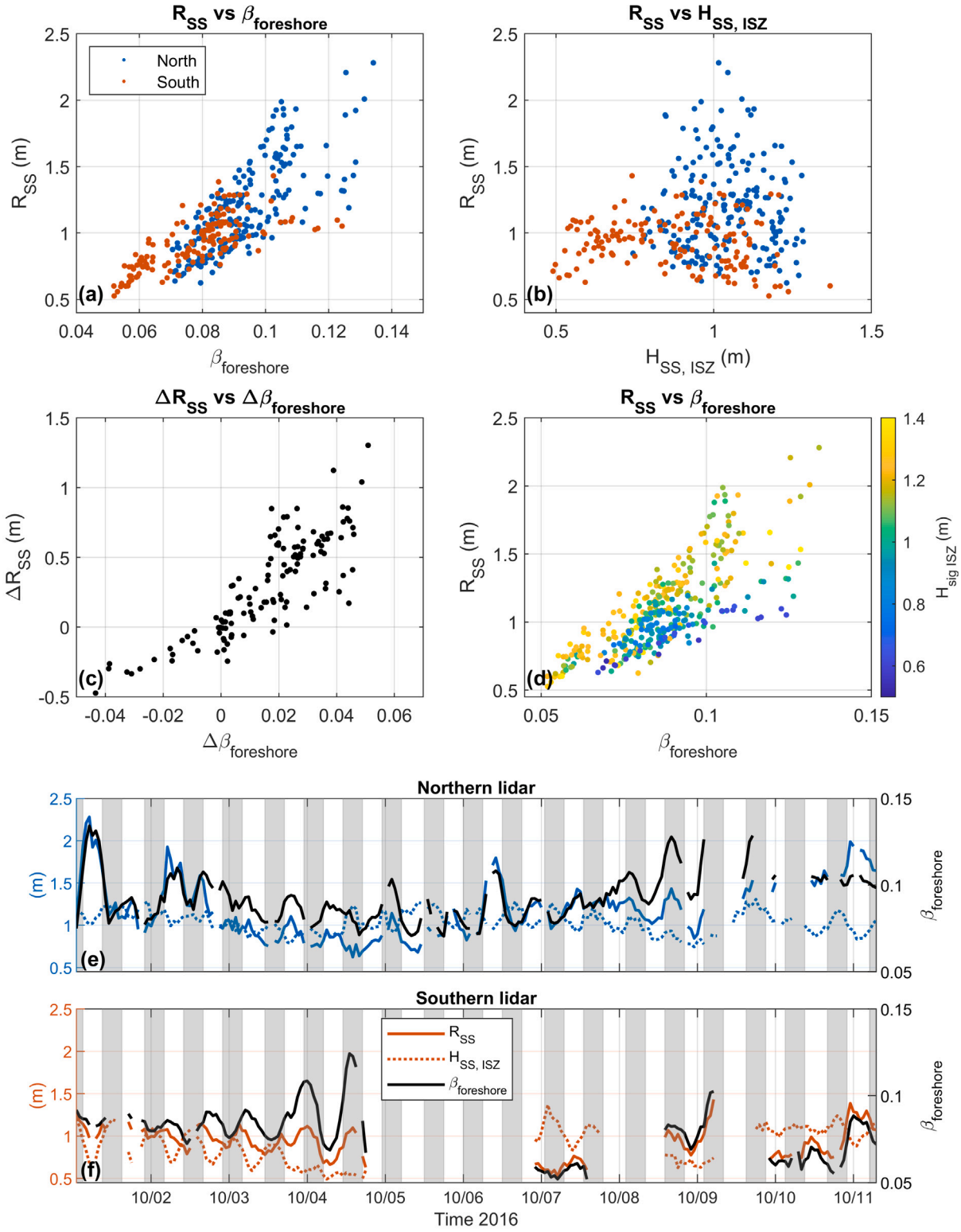

Fig. 8. R_{SS} versus (a) $\beta_{foreshore}$ and (b) $H_{SS,ISZ}$, (c) the difference R_{SS} versus the difference in $\beta_{foreshore}$, (d) R_{SS} versus $\beta_{foreshore}$ colored by $H_{sig,ISZ}$, and (e,f) R_{SS} (solid curves, axis on left), $H_{SS,ISZ}$ (dotted curves, axis on left), and $\beta_{foreshore}$ (black curves, axis on right) at the (e) northern (blue) and (f) southern (red) lidars.

the subtle differences in surfzone breaking patterns appear to influence strongly the inner surfzone wave energy at the two locations.

Consistent with prior studies (Guedes et al., 2011; Khoury et al., 2019), the runup dynamics were related to the changes in $H_{sig,ISZ}$ through the tidal cycle. The temporal trends in all runup quantities excluding R_{SS} had a similar peak near high tide at the southern lidar during low to moderate waves. Similar to $H_{SS,ISZ}$, alongshore differences in R_{mean} and R_T between the two locations were largest during low incident wave conditions, with the difference between R_{mean} at the two locations ranging from 0.00 to 0.45 m (compared with 0.00 to 0.24 m during times with larger wave heights, Fig. 12b) and differences in R_T ranging from 0.00 to 0.97 m (compared with 0.00 to 0.45 m

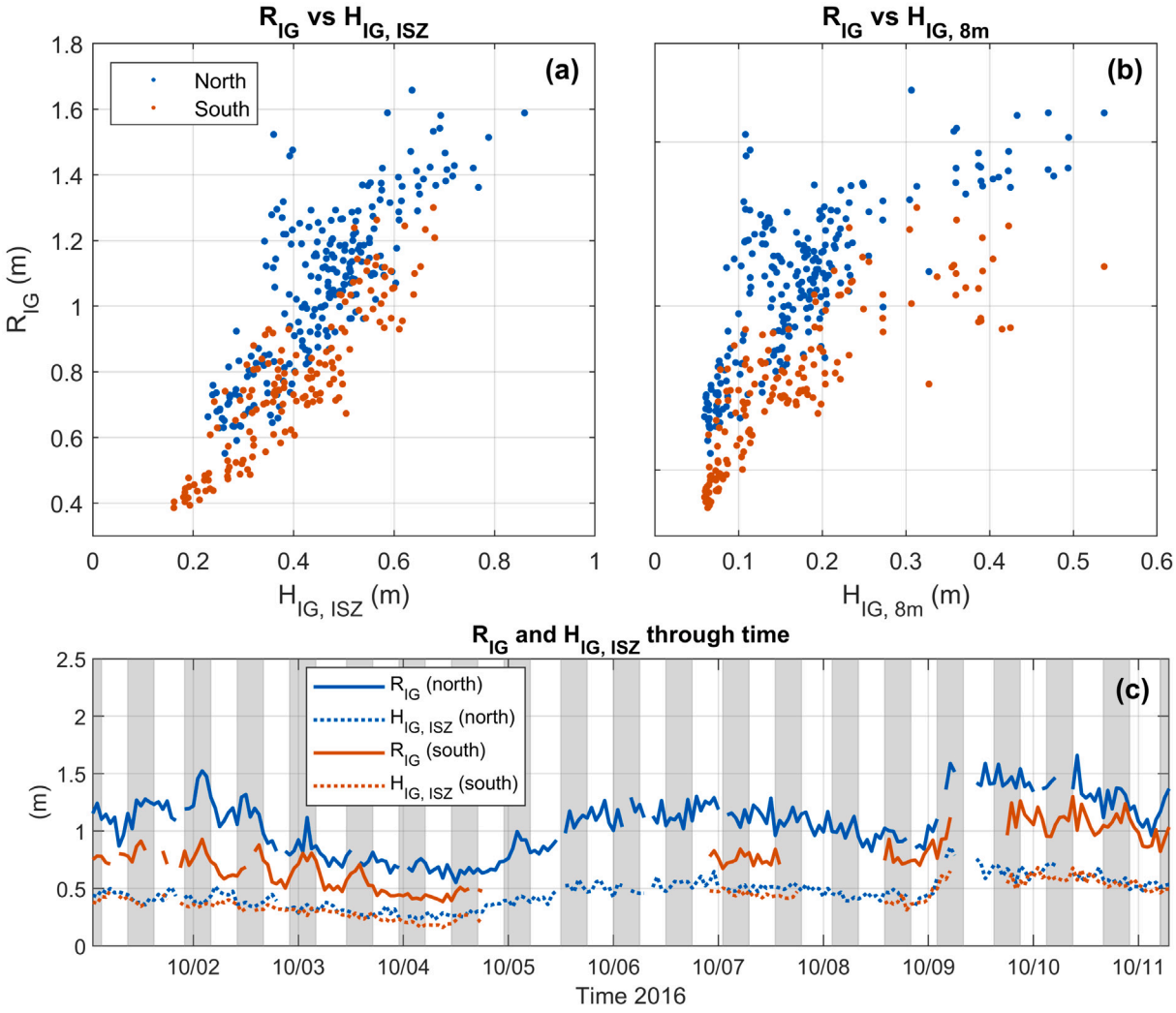

Fig. 9. R_{IG} versus (a) $H_{IG,ISZ}$ and (b) $H_{IG,8\ m}$, and (c) R_{IG} (solid curves) and $H_{IG,ISZ}$ (dash-dotted curves) at the northern (blue) and southern (red) lidars.

during times with larger wave heights, Fig. 12c). Temporal and spatial changes in R_{SS} were predominantly influenced by $\beta_{foreshore}$ variations due to tidally-varying swashzone locations and alongshore variability in beach morphology (Fig. 8). The changes in $\beta_{foreshore}$ through the tidal cycle at the southern lidar location were not in phase with the tide, with $\beta_{foreshore}$ often maximum during the falling tide.

The largest alongshore differences in several runup parameters ($\Delta R_{2\%}$ = 0.90 m, Fig. 12d, ΔR_{sig} = 1.23 m, and ΔR_T = 0.97 m, Fig. 12c) occurred on October 1 05:00 UTC at low tide, when surfzone wave heights were larger at the northern lidar location ($H_{sig,ISZ}$ = 1.15 m) than at the southern lidar location ($H_{sig,ISZ}$ = 0.84 m). In addition, the beach slope was steeper at the northern lidar location ($\beta_{foreshore}$ = 0.13) than at the southern lidar location ($\beta_{foreshore}$ = 0.08). The combination of alongshore differences in beach morphology (resulting in larger swash energy at the northern lidar location) and alongshore differences in surfzone bathymetry (resulting in larger inner surfzone wave energy at the northern lidar location) amplified the resulting alongshore differences in both the mean and oscillatory components of runup at the two locations.

4.1.2. October 9–10

When incident waves were large during the peak of Hurricane Matthew (Oct 9–10), $H_{SS,ISZ}$ values were significantly smaller than $H_{SS,8\ m}$ ($0.18 < H_{SS,ISZ}/H_{SS,8\ m} < 0.39$) and inner surfzone and runup parameters were more similar at the two lidar locations than they were earlier in the month during smaller wave conditions (Fig. 12). The inner surf wave heights exhibited distinct populations as the storm strengthened (early on October 9, Fig. 14a, blue dots at $H_{SS,8\ m} > 2.6$ m and $H_{SS,ISZ} < 0.95$ m and Fig. 14b, blue dots with $\theta_m < 0°$) and weakened (midday on October 9 through midday on October 10, Fig. 14a, green and orange dots at $H_{SS,8\ m} > 2.6$ m and $H_{SS,ISZ} > 0.95$ m, and Fig. 14b, yellow and green dots with $\theta_m > 0°$). Early on Oct 9, the mean wave direction ranged from −22 to −3.7°, meaning that the waves were approaching from the south and thus through the pier. Dissipation by the pier pilings and refraction over the bathymetric depression under the pier could contribute to reduced inner surfzone wave energy (Elgar et al., 2001). Although the reduction in $H_{SS,ISZ}$ early on October 9 is notable at both lidar locations, it is particularly pronounced at the southern lidar, with mean $H_{SS,ISZ}$ values of 0.69 m and 0.86 m at the southern and northern locations, respectively (Fig. 5e), and likely would be a source of increased variability in inner surfzone and runup parameters between the two lidar locations with certain wave incidence angles. As the storm passed offshore and mean wave directions became more northerly (Figs. 14b and 4c) the influence of the pier and associated bathymetry may have had less of an effect.

4.2. Comparison with literature

Alongshore variations in significant runup height R_{sig} may be owing to differences in foreshore slope (Ruggiero et al., 2004; Guedes et al.,

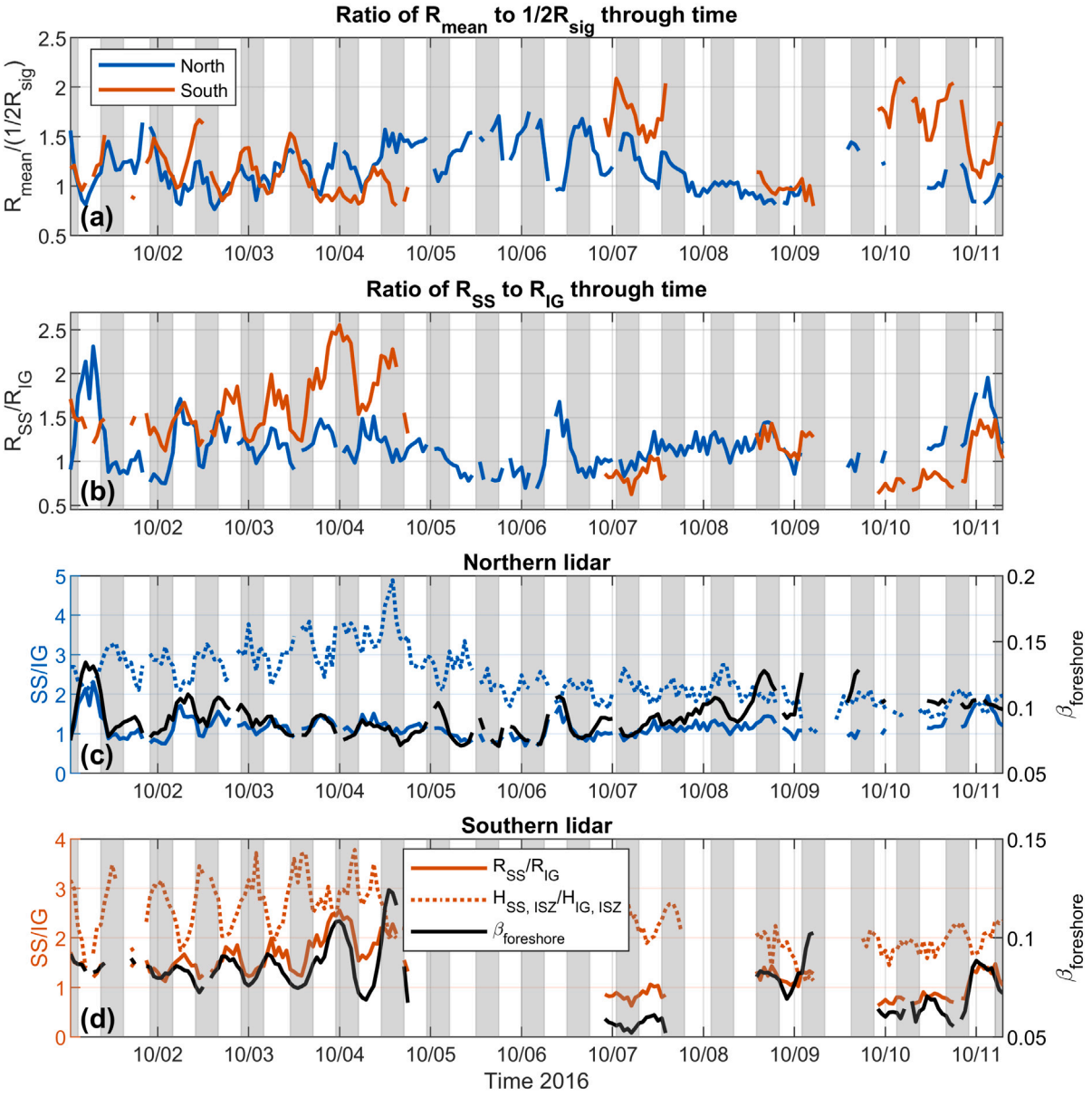

Fig. 10. Ratio of (a) R_{mean} to $\frac{1}{2}R_{sig}$ and (b) of R_{SS} to R_{IG} at the northern (blue) and southern (red) lidars, and (c,d) ratio of R_{SS} to R_{IG} (blue and red solid curves), ratio of $H_{SS,ISZ}$ to $H_{IG,ISZ}$ (blue and red dotted curves, axis on left) and $\beta_{foreshore}$ (black curves, axis on right) at the (c) northern (blue) and (d) southern (red) lidars versus time.

2012) or inner surfzone morphology (Senechal et al., 2018). Here, differences in R_{sig} and R_{SS} at the two locations are correlated with the differences in $\beta_{foreshore}$ (R^2 = 0.53 and R^2 = 0.70, respectively). However, extreme runup elevations ($R_{2\%}$) and the combined elevations of the mean runup and the oscillatory swash (R_T) are uncorrelated with $\beta_{foreshore}$ (R^2 = 0.02 and 0.02, respectively). These results suggest that although alongshore variations in $\beta_{foreshore}$ influence the alongshore variability in the magnitude of swash oscillations, they play a smaller role in the alongshore differences in the total elevation reached by runup on intermediate beaches.

On intermediate and dissipative beaches, runup saturation often occurs across the sea-swell frequency band, with some work showing runup saturation extending into infragravity frequencies in highly-dissipative conditions (Ruessink et al., 1998; Ruggiero et al., 2004; Senechal et al., 2011; De Bakker et al., 2014; Fiedler et al., 2015). The saturated frequency bands typically exhibit a f^{-4} (Raubenheimer and Guza, 1996; Ruggiero et al., 2001; Hughes et al., 2014) or more rarely f^{-3} (Guza and Thornton, 1982; Ruessink et al., 1998) energy roll-off, with the lowest saturated frequency a function of both beach type and offshore conditions (Hughes et al., 2014). In intermediate or dissipative conditions, runup spectral energy often roughly is constant across infragravity frequencies (Raubenheimer and Guza, 1996; Ruggiero et al., 2004). Here, the runup spectra exhibited similar behavior, with a relatively flat spectral shape at infragravity frequencies and a f^{-4} energy roll-off at frequencies above approximately f = 0.1 Hz (Fig. 15b). Consistent with previous results (Raubenheimer and Guza, 1996), the inner-surf spectra did not exhibit a similar energy falloff at higher frequencies (Fig. 15a). The magnitude of the extreme runup elevations $R_{2\%}$ and R_T correlated strongly with the inner-surf significant wave height integrated over all frequencies below the average lower limit of the saturated runup frequencies (approximately f = 0.1 Hz over the entire dataset, vertical dot-dashed line in Fig. 15) (R^2 = 0.81 and 0.84, respectively). These results suggest that while inner-surf spectra often contain comparable energy at frequencies above and below the lowest saturated frequency from the runup spectra, extreme runup correlates best to inner-surf energy from only unsaturated runup

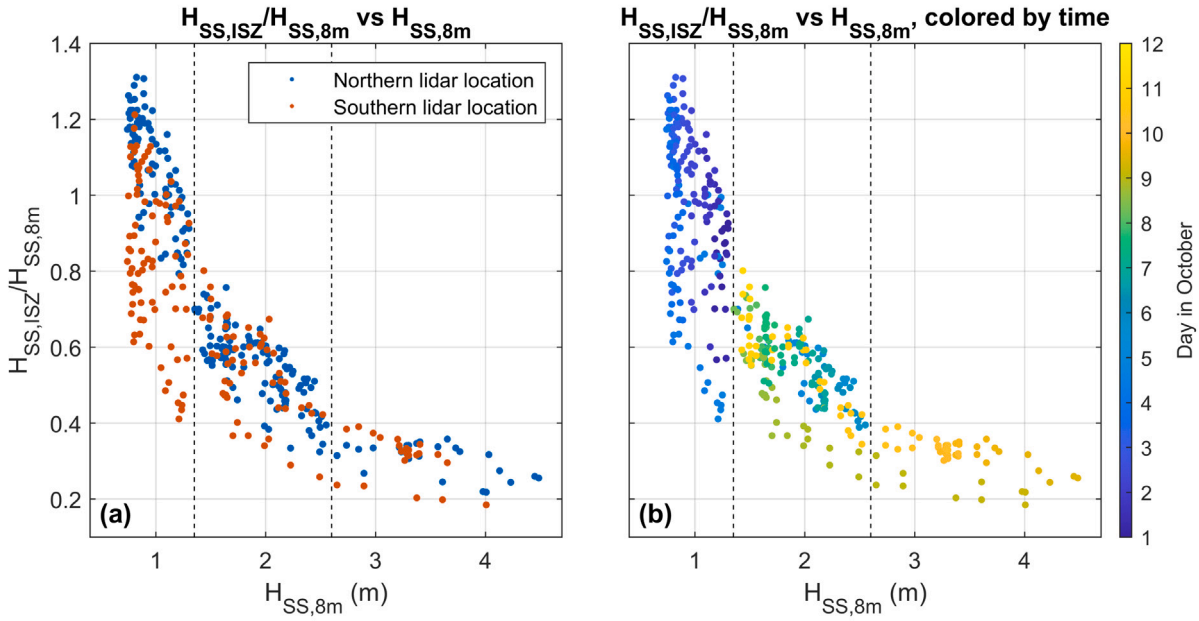

Fig. 11. The ratio of $H_{SS,ISZ}$ to $H_{SS,8\ m}$ versus $H_{SS,8\ m}$, colored by (a) lidar location and (b) day in October. The dotted lines indicate $H_{SS,8\ m}$ values of 1.35 and 2.60 m.

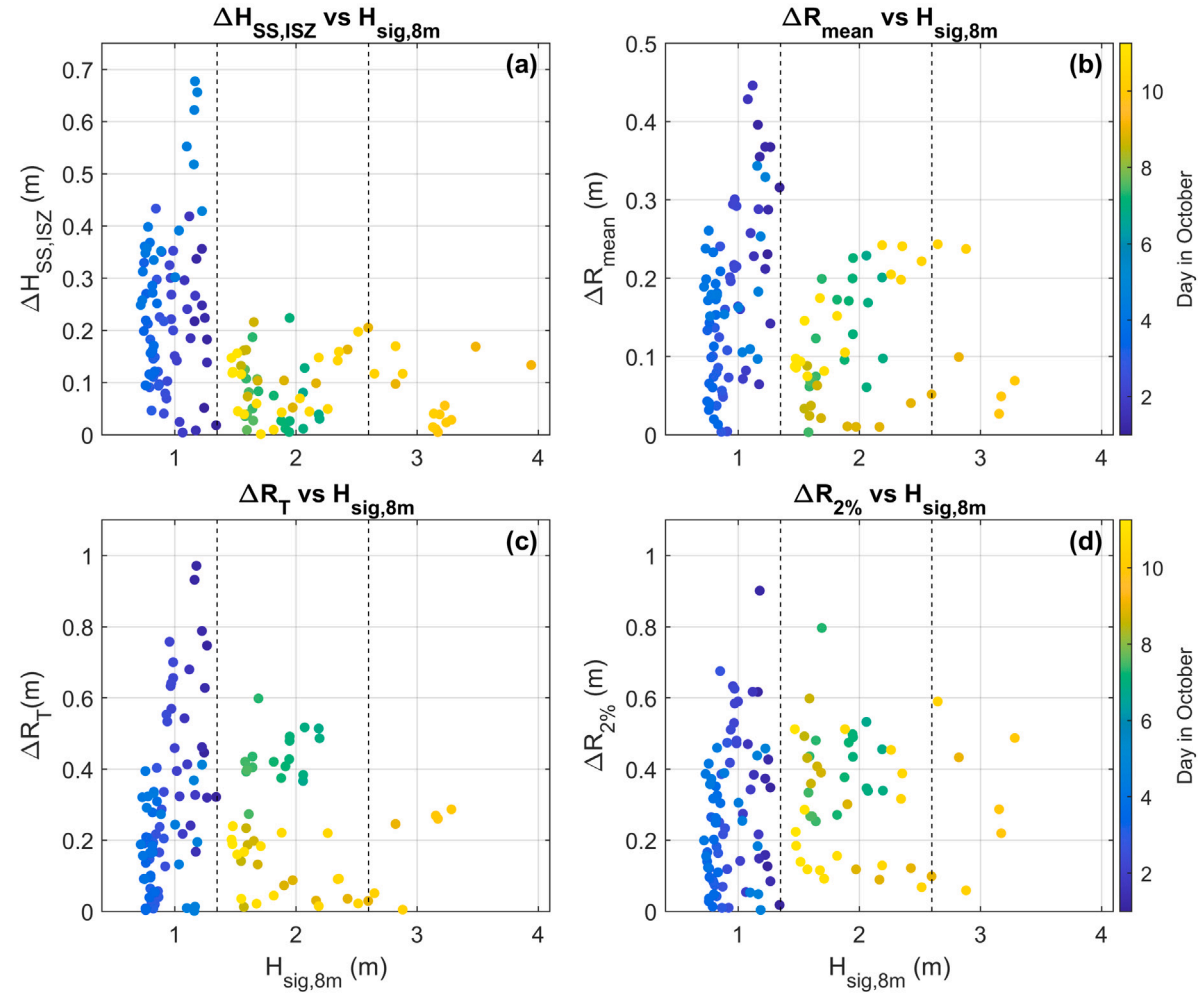

Fig. 12. The absolute difference between the value measured at the northern and southern lidar locations (indicated with a Δ) of (a) $H_{SS,ISZ}$, (b) R_{mean}, (c) R_T, and (d) $R_{2\%}$ versus $H_{sig,8\ m}$, colored by the day in October (scale on the right).

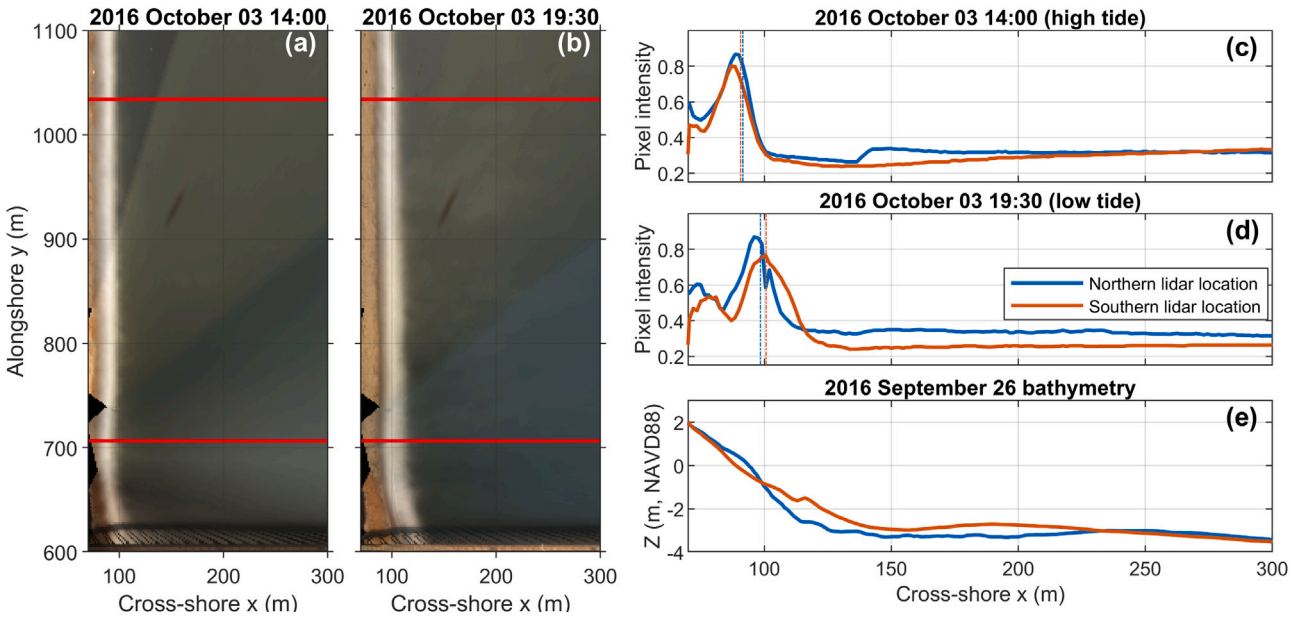

Fig. 13. (a and b) ARGUS time-averaged optical imagery as a function of alongshore and cross-shore distance and (c and d) pixel intensity at the north (blue) and south (red) lidar locations versus cross-shore distance on 3 October 2016 at (a and c) 14:00 (high tide) and (b and d) 19:30 (low tide), and (e) seafloor elevation versus cross-shore distance on September 26 2016 at the north (blue) and south (red) lidar locations.

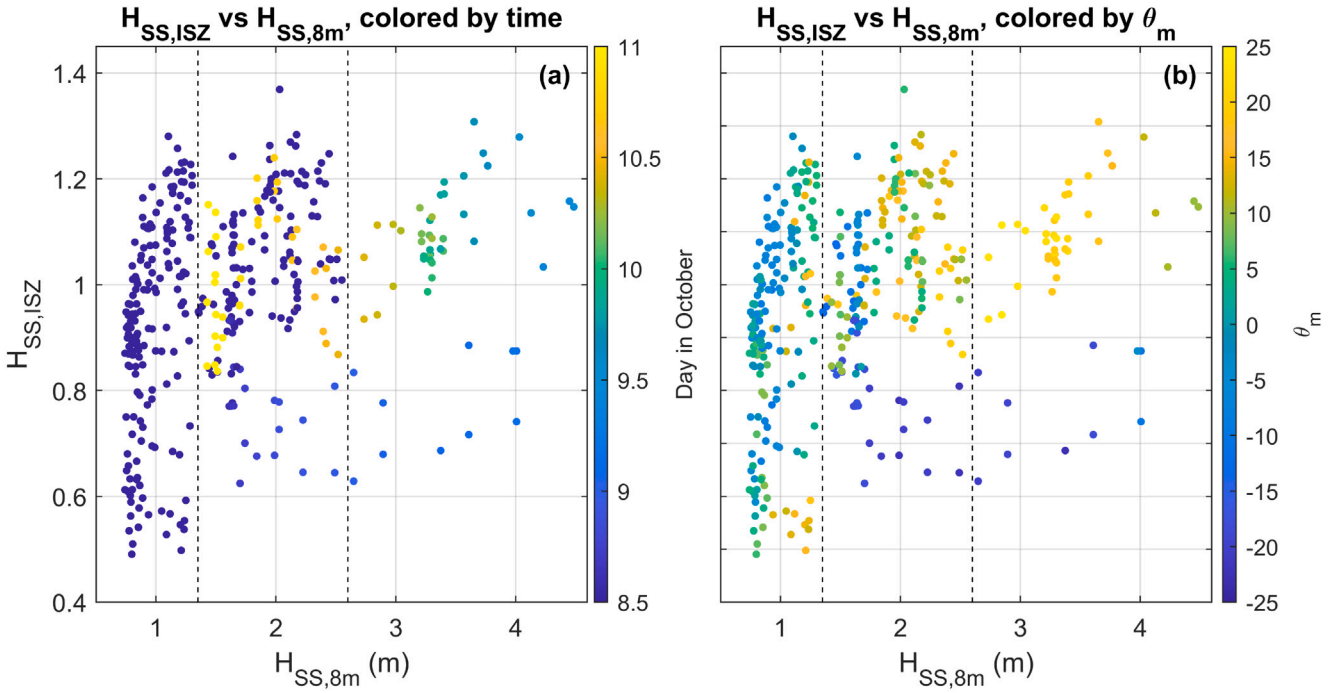

Fig. 14. $H_{SS,ISZ}$ versus $H_{SS,8\ m}$, colored by (a) the day in October and (b) the mean wave direction at the 8-m array (θ_m). Wave directions are given in a Cartesian coordinate system, with 0 indicating shore normal, positive values indicating an approach from the North, and negative values indicating an approach from the South.

frequencies. This cutoff frequency is thus dependent on both beach and offshore conditions, which may complicate efforts to develop universal parameterizations.

The mean runup elevation R_{mean} is influenced by both cross-shore gradients in radiation stresses due to wave breaking (wave-breaking-induced setup) and asymmetries in swash uprush relative to downrush on the beachface (Nielsen, 1989; Gourlay, 1992; O'Grady et al., 2019). Although the mean runup is often referred to as setup, the mean runup and the mean water surface elevation just outside of the swash zone Z_{mean} are correlated only weakly (R^2 = 0.23), with a much stronger correlation between R_{mean} and the significant wave height in the inner surf zone $H_{sig,ISZ}$ (R^2 = 0.72). These results suggest that the surfzone bathymetry is indirectly impacting R_{mean} via breaking wave dissipation that reduces $H_{sig,ISZ}$, whereas the contribution to R_{mean} from breaking-wave-induced setup may be relatively small.

Many parameterizations have been developed to estimate wave runup and its mean and oscillatory components (da Silva et al., 2020). Typically, the parameterizations rely on deep water wave conditions and foreshore beach slope, including the commonly-used Stockdon parameterization (Stockdon et al., 2006), and thus cannot account

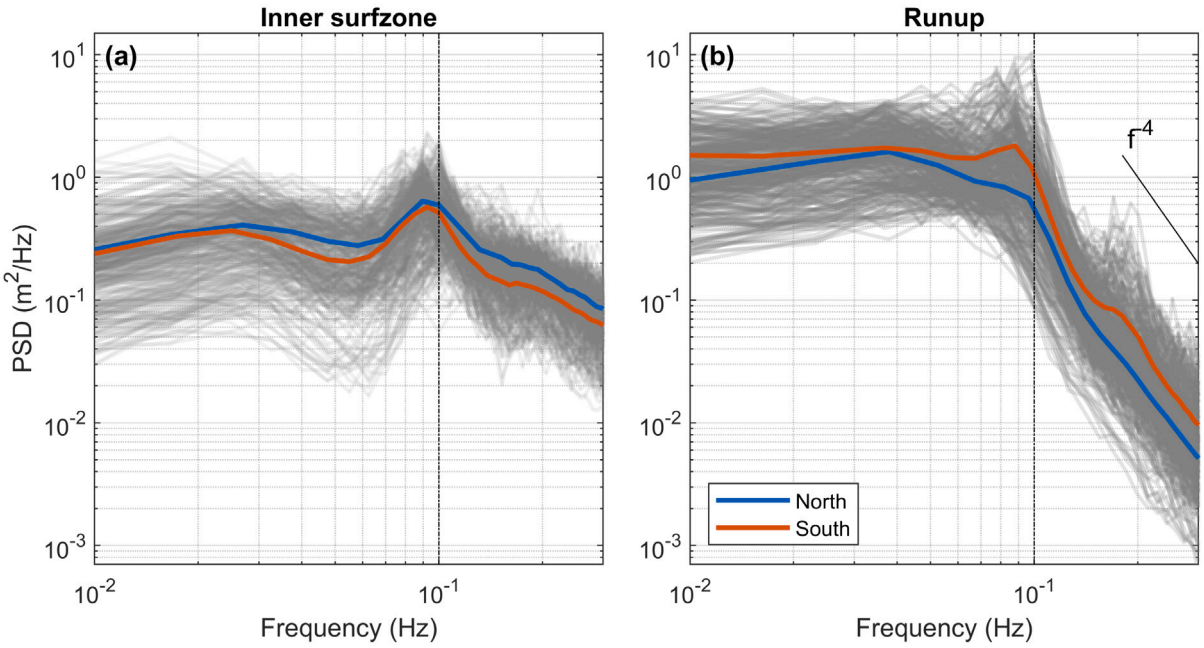

Fig. 15. Power spectral density of (a) inner surfzone and (b) runup spectra versus frequency from every hourly collect (gray) and averaged over the entire deployment period at the northern (blue) and southern (red) lidar locations. The vertical dot-dashed lines indicate the $f = 0.1$ Hz frequency cutoff.

for the influence of surfzone bathymetry on wave runup. Here, the observations were correlated with $R_{2\%}$ estimated using the Stockdon parameterization, as well as three other parameterizations that relate $R_{2\%}$ directly to $\sqrt{H_0 L_0}$ (Nielsen and Hanslow, 1991), $\sqrt{\beta_{foreshore} H_0 L_0}$ (Medellín et al., 2016), and $\beta_{foreshore}\sqrt{H_0 L_0}$ (Atkinson et al., 2017) ($0.53 < R^2 < 0.61$). However, the published coefficients for each parameterization resulted in large biases in $R_{2\%}$ ranging from 0.80–0.89 m over the entire dataset. Furthermore, although these parameterizations correlated relatively well with the observations, they did not include alongshore variability or temporal variability on the scale of individual tidal cycles, which mostly is controlled by the surfzone bathymetry.

4.3. Sources of error

There are several potential sources of error in the runup and inner surfzone parameters derived from the lidar datasets that could contribute to the observed scatter in the relationships. Poor rectification in the automated lidar processing can result in errors in the elevations of extracted parameters. Both lidar scanners were deployed on towers for extended periods and during extreme conditions, and some movement was visible between scans from hour to hour due to motion of the tower itself or thermal expansion of the base on which the scanner was mounted. An automated co-registration algorithm (O'Dea et al., 2019) was applied that aligned all scans to a defined baseline to remove this movement, and the scan alignment was then manually quality controlled. However, it is possible that rectification errors persisted in the final data set, which could result in some scatter, primarily in parameters that rely on absolute elevation values ($R_{2\%}$, R_{mean}, and Z_{mean}). Analyses of elevation time series from fixed locations on the dune that were not impacted by wave action showed a vertical point spread of about 0.05 m over the deployment period. In addition, the location of the 0.5-m contour was estimated by linearly extending the beach slope beyond the measured extent through the swash zone. Inner surfzone parameters are depth dependent, and thus could be impacted by errors in the estimated location of the 0.5-m depth contour.

Runup digitization is an additional potential source of error. The manual runup digitization process used in this study is subjective and could result in some variability in the extracted runup position. The digitization was conducted using timestacks of lidar reflectance, elevation, and elevation difference from a minimum value. Although there is little ambiguity in the position of runup during the wave uprush, wave rundown often is defined less clearly and therefore more susceptible to different interpretations. Since the collection and processing of this dataset in 2016 and 2017, new methods for collecting data and extracting runup location and elevation have been developed. Drone-mounted lidars (Fiedler et al., 2021) and low cost lidar systems (O'Connor and Mieras, 2022) expand the range of conditions in which data can be collected. New runup digitization methodologies that rely on machine learning algorithms have been developed that facilitate the processing of large lidar-based (Collins et al., 2023) and video-based (Buckley et al., 2024; Salatin et al., 2024; van der Grinten et al., 2025) datasets. Additionally, new runup extraction methodologies that define the runup location as the estimated location of an instantaneous depth contour using lidar-derived data products provide more quantitative definition of runup and remove the subjectivity inherent in the manual digitization process (Fiedler et al., 2021; Collins et al., 2023). To determine whether the methods used in the present study were affecting the results, a contour-based runup extraction methodology (Collins et al., 2023) was applied to the northern lidar dataset and the resulting runup parameters were compared. The $R_{2\%}$ and R_{mean} datasets derived using the two runup extraction methodologies applied to the same dataset had correlation coefficients $R^2 = 0.98$ and 0.99, respectively, suggesting that the manual digitization process used here is not influencing the results significantly.

5. Conclusions

Observations of runup and inner surfzone hydrodynamics were collected for 11 days in October 2016 before, during, and after Hurricane Matthew on an intermediate beach using two lidar scanners separated by ~330 m in the alongshore at the U.S. Army Engineer Research and Development Center Field Research Facility. The ratio of the significant sea-swell wave height in the inner surf zone to that in about 8-m

water depth $H_{SS,ISZ}/H_{SS,8\ m}$ ranged from 0.42 to 1.31 during low-energy conditions (total offshore wave heights $H_{sig,8\ m} < 1.35$ m) and from 0.19 to 0.80 during high-energy conditions ($1.35 < H_{sig,8\ m} < 4.6$ m) when inner-surf wave heights were limited by wave breaking. Alongshore variability of $H_{SS,ISZ}$, the mean runup R_{mean}, and the combined mean runup and significant swash amplitude R_T was largest during low-energy incident conditions when sea-swell energy was unsaturated in the inner surf zone. However, the extreme runup $R_{2\%}$ exhibited alongshore variability for a wider range of wave conditions. The mean runup R_{mean} was weakly correlated with the mean water surface elevation in the inner surf zone Z_{mean} ($R^2 = 0.23$), suggesting that changes in water surface elevation due to wave-breaking-induced setup is only one factor contributing to R_{mean}. Consistent with prior studies (Raubenheimer and Guza, 1996; Ruggiero et al., 2004; Stockdon et al., 2006), the magnitude of swash oscillation in the sea swell band R_{SS} was related to the foreshore beach slope $\beta_{foreshore}$, and alongshore differences in the significant sea-swell swash height R_{SS} and the total significant swash height R_{sig} were correlated with alongshore differences in $\beta_{foreshore}$ ($R^2 = 0.70$ and $R^2 = 0.53$, respectively). However, the alongshore differences in R_{mean} were correlated more strongly with the alongshore differences in the total inner surf wave height $H_{sig,ISZ}$, which is controlled by incident wave conditions and wave dissipation patterns across the surf zone. These results suggest that on intermediate beaches $\beta_{foreshore}$ influences the magnitude of swash oscillations but has a smaller role in the elevation reached by the extreme and mean runup, which is affected more strongly by spatial and temporal variations in inner surfzone wave heights. Thus, these results demonstrate the importance of both beach and surfzone morphology in the extent and oscillatory dynamics of wave runup on intermediate beaches.

CRediT authorship contribution statement

Annika O'Dea: Writing – original draft, Visualization, Validation, Methodology, Investigation, Formal analysis, Data curation, Conceptualization. **Britt Raubenheimer:** Writing – review & editing, Supervision, Resources, Methodology, Funding acquisition, Formal analysis, Conceptualization. **Katherine Brodie:** Writing – review & editing, Supervision, Resources, Project administration, Methodology, Funding acquisition, Formal analysis, Conceptualization. **Steve Elgar:** Writing – review & editing, Supervision, Resources, Methodology, Funding acquisition, Formal analysis, Conceptualization.

Declaration of competing interest

The authors declare that they have no known competing financial interests or personal relationships that could have appeared to influence the work reported in this paper.

Acknowledgments

The authors thank staff at the US Army Corps of Engineers Field Research Facility and the Woods Hole Oceanographic Institution PVLAB for deploying and maintaining the lidars and in situ instruments during a massive storm. Funding for this project was provided by the U.S. Army Corps of Engineers, USA' Coastal and Ocean Data Systems and Coastal Field Data Collection Programs, the National Science Foundation, USA, and a Vannevar Bush Faculty Fellowship, USA.

Data availability

Data will be made available on request.

References

Almeida, L.P., Almar, R., Blenkinsopp, C., Senechal, N., Bergsma, E., Floc'h, F., Caulet, C., Biausque, M., Marchesiello, P., Grandjean, P., et al., 2020. Lidar observations of the swash zone of a low-tide terraced tropical beach under variable wave conditions: The nha trang (Vietnam) coastvar experiment. J. Mar. Sci. Eng. 8 (302).

Atkinson, A.L., Power, H.E., Moura, T., Hammond, T., Callaghan, D.P., Baldock, T.E., 2017. Assessment of runup predictions by empirical models on non-truncated beaches on the South-East Australian coast. Coast. Eng. 119, 15–31.

Battjes, J.A., 1974. Surf similarity. In: Coastal Engineering 1974. pp. 466–480.

Blenkinsopp, C., Matias, A., Howe, D., Castelle, B., Marieu, V., Turner, I., 2016. Wave runup and overwash on a prototype-scale sand barrier. Coast. Eng. 113, 88–103.

Brodie, K., Conery, I., Cohn, N., Spore, N., Palmsten, M., 2019. Spatial variability of coastal foredune evolution, Part A: Timescales of months to years. J. Mar. Sci. Eng. 7, 124.

Brodie, K., Slocum, R.K., McNinch, J.E., 2012. New insights into the physical drivers of wave runup from a continuously operating terrestrial laser scanner. In: 2012 Oceans. IEEE, pp. 1–8.

Buckley, M.L., Buscombe, D., Birchler, J.J., Palmsten, M.L., Swanson, E., Brown, A., Harrison, S.R., 2024. Wave runup and total water level observations from time series imagery at several sites with varying nearshore morphologies. Coast. Eng. 193, 104600.

Chen, J., Raubenheimer, B., Elgar, S., 2024. Wave and roller transformation over barred bathymetry. J. Geophys. Res.: Ocean. 129, e2023JC020413.

Cohn, N., Brodie, K.L., Johnson, B., Palmsten, M.L., 2021. Hotspot dune erosion on an intermediate beach. Coast. Eng. 170, 103998.

Cohn, N., Ruggiero, P., 2016. The influence of seasonal to interannual nearshore profile variability on extreme water levels: Modeling wave runup on dissipative beaches. Coast. Eng. 115, 79–92.

Collins, A.M., O'Dea, A., Brodie, K.L., Bak, A.S., Hesser, T.J., Spore, N.J., Farthing, M.W., 2023. Automated extraction of a depth-defined wave runup time series from lidar data using deep learning. IEEE Trans. Geosci. Remote Sens. 61, 1–13.

Cox, N., Dunkin, L.M., Irish, J.L., 2013. An empirical model for infragravity swash on barred beaches. Coast. Eng. 81, 44–50.

da Silva, P.G., Coco, G., Garnier, R., Klein, A.H., 2020. On the prediction of runup, setup and swash on beaches. Earth-Sci. Rev. 204, 103148.

da Silva, P.G., Medina, R., Gonzalez, M., Garnier, R., 2019. Wave reflection and saturation on natural beaches: The role of the morphodynamic beach state in incident swash. Coast. Eng. 153, 103540.

De Bakker, A., Tissier, M., Ruessink, B., 2014. Shoreline dissipation of infragravity waves. Cont. Shelf Res. 72, 73–82.

Elgar, S., Guza, R., O'Reilly, W., Raubenheimer, B., Herbers, T., 2001. Wave energy and direction observed near a pier. J. Waterw. Port Coast. Ocean. Eng. 127, 2–6.

Fiedler, J.W., Brodie, K.L., McNinch, J.E., Guza, R.T., 2015. Observations of runup and energy flux on a low-slope beach with high-energy, long-period ocean swell. Geophys. Res. Lett. 42, 9933–9941.

Fiedler, J.W., Kim, L., Grenzeback, R.L., Young, A.P., Merrifield, M.A., 2021. Enhanced surf zone and wave runup observations with hovering drone-mounted lidar. J. Atmos. Ocean. Technol. 38 (11), 1967–1978.

Forte, M.F., Birkemeier, W.A., Mitchell, J.R., 2017. Nearshore Survey System Evaluation. Technical Report, ERDC-CHL Vicksburg, MS, United States.

Gourlay, M.R., 1992. Wave set-up, wave run-up and beach water table: Interaction between surf zone hydraulics and groundwater hydraulics. Coast. Eng. 17, 93–144.

Guedes, R., Bryan, K.R., Coco, G., 2012. Observations of alongshore variability of swash motions on an intermediate beach. Cont. Shelf Res. 48, 61–74.

Guedes, R., Bryan, K.R., Coco, G., Holman, R.A., 2011. The effects of tides on swash statistics on an intermediate beach. J. Geophys. Res.: Ocean. 116.

Guza, R., Bowen, A., 1977. Resonant interactions for waves breaking on a beach. In: Coastal Engineering 1976. pp. 560–579.

Guza, R., Thornton, E., 1982. Swash oscillations on a natural beach. J. Geophys. Res.: Ocean. 87, 483–491.

Guza, R., Thornton, E., Holman, R., 1985. Swash on steep and shallow beaches. In: Coastal Engineering 1984. pp. 708–723.

Holman, R., 1986. Extreme value statistics for wave run-up on a natural beach. Coast. Eng. 9, 527–544.

Holman, R., Sallenger, Jr., A., 1985. Setup and swash on a natural beach. J. Geophys. Res.: Ocean. 90, 945–953.

Holman, R., Stanley, J., 2007. The history and technical capabilities of argus. Coast. Eng. 54 (6–7), 477–491.

Hughes, M.G., Aagaard, T., Baldock, T.E., Power, H.E., 2014. Spectral signatures for swash on reflective, intermediate and dissipative beaches. Mar. Geol. 355, 88–97.

Hunt, Jr., I.A., 1959. Design of seawalls and breakwaters. J. Waterw. Harb. Div. 85, 123–152.

Huntley, D., Guza, R., Bowen, A., 1977. A universal form for shoreline run-up spectra? J. Geophys. Res. 82, 2577–2581.

Khoury, A., Jarno, A., Marin, F., 2019. Experimental study of runup for sandy beaches under waves and tide. Coast. Eng. 144, 33–46.

Long, C.E., Oltman-Shay, J.M., 1991. Directional Characteristics of Waves in Shallow Water. Technical Report, Coastal Engineering Research Center Vicksburg MS.

Medellín, G., Brinkkemper, J., Torres-Freyermuth, A., Appendini, C., Mendoza, E., Salles, P., 2016. Run-up parameterization and beach vulnerability assessment on a barrier island: A downscaling approach. Nat. Hazards Earth Syst. Sci. 16, 167–180.
Miche, M., 1951. Le pouvoir réfléchissant des ouvrages maritimes exposés à l'action de la houle. Ann. Ponts Chaussées 121, 285–319.
Moraes, C.d.C., 1970. Experiments of wave reflexion on impermeable slopes. In: Coastal Engineering 1970. pp. 509–521.
Nielsen, P., 1989. Wave setup and runup: An integrated approach. Coast. Eng. 13, 1–9.
Nielsen, P., Hanslow, D.J., 1991. Wave runup distributions on natural beaches. J. Coast. Res. 113, 9–1152.
O'Connor, C.S., Mieras, R.S., 2022. Beach profile, water level, and wave runup measurements using a standalone line-scanning, low-cost (llc) lidar system. Remote. Sens. 14 (19), 4968.
O'Dea, A., Brodie, K.L., Hartzell, P., 2019. Continuous coastal monitoring with an automated terrestrial lidar scanner. J. Mar. Sci. Eng. 7 (37).
O'Grady, J., McInnes, K., Hemer, M., Hoeke, R., Stephenson, A., Colberg, F., 2019. Extreme water levels for australian beaches using empirical equations for shoreline wave setup. J. Geophys. Res.: Ocean. 124, 5468–5484.
Palmsten, M.L., Splinter, K.D., 2016. Observations and simulations of wave runup during a laboratory dune erosion experiment. Coast. Eng. 115, 58–66.
Pianca, C., Holman, R., Siegle, E., 2015. Shoreline variability from days to decades: Results of long-term video imaging. J. Geophys. Res.: Ocean. 120, 2159–2178.
Raubenheimer, B., Guza, R., 1996. Observations and predictions of run-up. J. Geophys. Res.: Ocean. 101, 25575–25587.
Raubenheimer, B., Guza, R., Elgar, S., Kobayashi, N., 1995. Swash on a gently sloping beach. J. Geophys. Res.: Ocean. 100, 8751–8760.
Ruessink, B., Kleinhans, M., Van den Beukel, P., 1998. Observations of swash under highly dissipative conditions. J. Geophys. Res.: Ocean. 103, 3111–3118.
Ruggiero, P., Holman, R.A., Beach, R., 2004. Wave run-up on a high-energy dissipative beach. J. Geophys. Res.: Ocean. 109.
Ruggiero, P., Komar, P.D., McDougal, W.G., Marra, J.J., Beach, R.A., 2001. Wave runup, extreme water levels and the erosion of properties backing beaches. J. Coast. Res. 407–419.
Salatin, R., Chen, Q., Raubenheimer, B., Elgar, S., Gorrell, L., 2024. A new framework for quantifying alongshore variability of swash motion using fully convolutional networks. Coast. Eng. 192, 104542.
Senechal, N., Coco, G., Bryan, K.R., Holman, R.A., 2011. Wave runup during extreme storm conditions. J. Geophys. Res.: Ocean. 116.
Senechal, N., Coco, G., Plant, N., Bryan, K.R., Brown, J., MacMahan, J.H., 2018. Field observations of alongshore runup variability under dissipative conditions in the presence of a shoreline sandwave. J. Geophys. Res.: Ocean. 123, 6800–6817.
Serafin, K.A., Ruggiero, P., 2014. Simulating extreme total water levels using a time-dependent, extreme value approach. J. Geophys. Res.: Ocean. 119, 6305–6329.
Stockdon, H.F., Holman, R.A., Howd, P.A., Sallenger, Jr., A.H., 2006. Empirical parameterization of setup, swash, and runup. Coast. Eng. 53, 573–588.
Stockdon, H.F., Thompson, D.M., Plant, N.G., Long, J.W., 2014. Evaluation of wave runup predictions from numerical and parametric models. Coast. Eng. 92, 1–11.
van der Grinten, M.J., Christiaanse, J.C., Reniers, A.J., Taal, F., Figlus, J., Antolínez, J.A., 2025. Wave runup extraction on dissipative beaches: New video-based methods. Coast. Eng. 104757.
Wright, L.D., Short, A.D., 1984. Morphodynamic variability of surf zones and beaches: A synthesis. Mar. Geol. 56 (1–4), 93–118.